Banner appropriate to article type will appear here in typeset article

# A revised gap-averaged Floquet analysis of Faraday waves in Hele-Shaw cells

**Alessandro Bongarzone[1] †, Baptiste Jouron[1], Francesco Viola[2] and François Gallaire[1]**

[1]Laboratory of Fluid Mechanics and Instabilities, École Polytechnique Fédérale de Lausanne, Lausanne, CH-1015, Switzerland

[2]Gran Sasso Science Institute, Viale F. Crispi, 7, 67100 L'Aquila, Italy

(Received xx; revised xx; accepted xx)

Existing theoretical analyses of Faraday waves in Hele-Shaw cells rely on the Darcy approximation and assume a parabolic flow profile in the narrow direction. However, Darcy's model is known to be inaccurate when convective or unsteady inertial effects are important. In this work, we propose a gap-averaged Floquet theory accounting for inertial effects induced by the unsteady terms in the Navier-Stokes equations, a scenario that corresponds to a pulsatile flow where the fluid motion reduces to a two-dimensional oscillating Poiseuille flow, similarly to the Womersley flow in arteries. When gap-averaging the linearised Navier-Stokes equation, this results in a modified damping coefficient, which is a function of the ratio between the Stokes boundary layer thickness and the cell's gap, and whose complex value depends on the frequency of the wave response specific to each unstable parametric region. We first revisit the standard case of horizontally infinite rectangular Hele-Shaw cells by also accounting for a dynamic contact angle model. A comparison with existing experiments shows the predictive improvement brought by the present theory and points out how the standard gap-averaged model often underestimates the Faraday threshold. The analysis is then extended to the less conventional case of thin annuli. A series of dedicated experiments for this configuration highlights how Darcy's thin-gap approximation overlooks a frequency detuning that is essential to correctly predict the locations of the Faraday tongues in the frequency-amplitude parameter plane. These findings are well rationalised and captured by the present model.

## 1. Introduction

Recent Hele-Shaw cell experiments have enriched the knowledge of Faraday waves (Faraday 1831). Researchers have uncovered a new type of highly localised standing waves, referred to as oscillons, that are both steep and solitary-like in nature (Rajchenbach *et al.* 2011). These findings have spurred further experimentations with Hele-Shaw cells filled with one or more liquid layers, using a variety of fluids, ranging from silicone oil and water-ethanol mixtures to pure ethanol (Li *et al.* 2018*b*). Through these experiments, new combined patterns produced by triadic interactions of oscillons were discovered by Li *et al.* (2014). Additionally, another new family of waves was observed in a cell filled solely with pure ethanol and at extremely

† Email address for correspondence: alessandro.bongarzone@epfl.ch

Abstract must not spill onto p.2

shallow liquid depths (Li *et al.* 2015, 2016).

All these findings contribute to the understanding of the wave behaviour in Hele-Shaw configurations and call for a reliable stability theory that can explain and predict the instability onset for the emergence of initial wave patterns.

Notwithstanding two-dimensional direct numerical simulations (Périnet *et al.* 2016; Ubal *et al.* 2003) have been able to qualitatively replicate standing wave patterns reminiscent of those observed in experiments (Li *et al.* 2014), these simulations overlook the impact of wall attenuation, hence resulting in a simplified model that cannot accurately predict the instability regions (Benjamin & Ursell 1954; Kumar & Tuckerman 1994) and is therefore not suitable for modelling Hele-Shaw flows. On the other hand, attempting to conduct three-dimensional simulations of fluid motions in a Hele-Shaw cell poses a major challenge due to the high computational cost associated with the narrow dimension of the cell, which requires a smaller grid cell size to capture the shear dissipation accurately. Consequently, the cost of performing such simulations increases rapidly as the cell gap narrows.

In order to tackle the challenges associated with resolving fluid dynamics within such systems, researchers have utilised Darcy's law as an approach to treating the confined fluid between two vertical walls. This approximation, also used in the context of porous media, considers the fluid to be flowing through a porous medium, resulting in a steady parabolic flow in the short dimension. When gap-averaging the linearised Navier-Stokes equation, this approximation translates into a damping coefficient $\sigma$ that scales as $12\nu/b^2$, with $\nu$ the fluid kinematic viscosity and $b$ the cell's gap-size, which represents the boundary layer dissipation at the lateral walls. However, Darcy's model is known to be inaccurate when convective and unsteady inertial effects are not negligible, such as in waves (Kalogirou *et al.* 2016). It is challenging to reintroduce convective terms consistently into the gap-averaged Hele-Shaw equations from a mathematical standpoint (Ruyer-Quil 2001; Plouraboué & Hinch 2002; Luchini & Charru 2010).

In their research, Li *et al.* (2018*a*) applied the Kelvin-Helmholtz-Darcy theory proposed by Gondret & Rabaud (1997) to reintroduce advection and derive the nonlinear gap-averaged Navier-Stokes equations. These equations were then implemented in the open-source code *Gerris* developed by Popinet (2003, 2009) to simulate Faraday waves in a Hele-Shaw cell. Although this gap-averaged model was compared to several experiments and demonstrated fairly good agreement, it should be noted that the surface tension term remains two-dimensional, as the out-of-plane interface shape is not directly taken into account. Recently, Rachik & Aniss (2023) have studied the effects of finite depth and surface tension on the linear and weakly nonlinear stability of the Faraday waves in Hele-Shaw cells, but the out-of-plane curvature was not retained. This simplified treatment neglects the contact line dynamics and may lead to miscalculations in certain situations. Advances in this direction were made by Li *et al.* (2019), who found that the out-of-plane capillary forces associated with the meniscus curvature across the thin-gap direction should be retained in order to improve the description of the wave dynamics, as experimental evidence suggests. By employing a more sophisticated model, coming from molecular kinetics theory (Blake 1993; Hamraoui *et al.* 2000; Blake 2006) and similar to the macroscopic model introduced by Hocking (1987), they included the capillary contact line motion arising from the small scale of the gap-size between the two walls of a Hele-Shaw cell and they derived a novel dispersion relation, which indeed better predicts the observed instability onset.

However, discrepancies in the instability thresholds were still found. This mismatch was tentatively attributed to factors that are not accounted for in the gap-averaged model, such as the extra dissipation on the lateral walls in the elongated direction. Of course, a lab-scale experiment using a rectangular cell cannot entirely replace an infinite-length model. Still, if the container is sufficiently long, this extra dissipation should be negligible. Other candidates for the mismatch between theory and experiments were identified in the phenomenological contact line model or free surface contaminations.

If these factors can certainly be sources of discrepancies, we believe that a pure hydrodynamic effect could be at the origin of the discordance between theory and experiments in the first place.

Despite the use of the Darcy approximation is well-assessed in the literature, the choice of a steady Poiseuille flow profile as an ansatz to build the gap-averaged model appears in fundamental contrast with the unsteady nature of oscillatory Hele-Shaw flows, such as Faraday waves. At low enough oscillation frequencies or for sufficiently viscous fluids, the thickness of the oscillating Stokes boundary layer becomes comparable to the cell gap: the Stokes layers over the lateral solid faces of the cell merge and eventually invade the entire fluid bulk. The Poiseuille profile gives an adequate flow description in such scenarios, but this pre-requisite is rarely met in the above-cited experimental campaigns. It appears, thus, very natural to ask oneself whether a more appropriate description of the oscillating boundary layer impacts the prediction of stability boundaries. This study is precisely devoted to answering this question by proposing a revised gap-averaged Floquet analysis based on the classical Womersley-like solution for the pulsating flow in a channel (Womersley 1955; San & Staples 2012).

Following the approach taken by Viola *et al.* (2017), we examine the impact of inertial effects on the instability threshold of Faraday waves in Hele-Shaw cells, with a focus on the unsteady term of the Navier-Stokes equations. This scenario corresponds to a pulsatile flow where the fluid's motion reduces to a two-dimensional oscillating channel flow, which seems better suited than the steady Poiseuille profile to investigate the stability properties of the system. When gap-averaging the linearised Navier-Stokes equation, this results in a modified damping coefficient becoming a function of the ratio between the Stokes boundary layer thickness and the cell's gap, and whose complex value will depend on the frequency of the wave response specific to each unstable parametric region.

First, we consider the case of horizontally infinite rectangular Hele-Shaw cells by also accounting for the same dynamic contact angle model employed by Li *et al.* (2019) so as to quantify the predictive improvement brought by the present theory. A *vis*-à-vis comparison with experiments by Li *et al.* (2019) points out how the standard Darcy model often underestimates the Faraday threshold. In contrast, the present theory can explain and close the gap with these experiments.

The analysis is then extended to the case of thin annuli. This less common configuration has already been used to investigate oscillatory phase modulation of parametrically forced surface waves (Douady *et al.* 1989) and drift instability of cellular patterns (Fauve *et al.* 1991). For our interest, an annular cell is convenient as it naturally filters out the extra dissipation that could take place on the lateral boundary layer in the elongated direction, hence allowing us to reduce the sources of extra uncontrolled dissipation and perform a cleaner comparison with experiments. Our homemade experiments for this configuration highlight how Darcy's theory overlooks a frequency detuning that is essential to correctly predict the locations of the Faraday's tongues in the frequency spectrum. These findings are well rationalised and captured by the present model.

The paper is organised as follows. In §2, we revisit the classical case of horizontally infinite rectangular Hele-Shaw cells. The present model is compared with theoretical predictions from the standard Darcy theory and existing experiments. The case of thin annuli is then considered. The model for the latter unusual configuration is formulated in §3 and compared with homemade experiments in §4. Conclusions are outlined in §5.

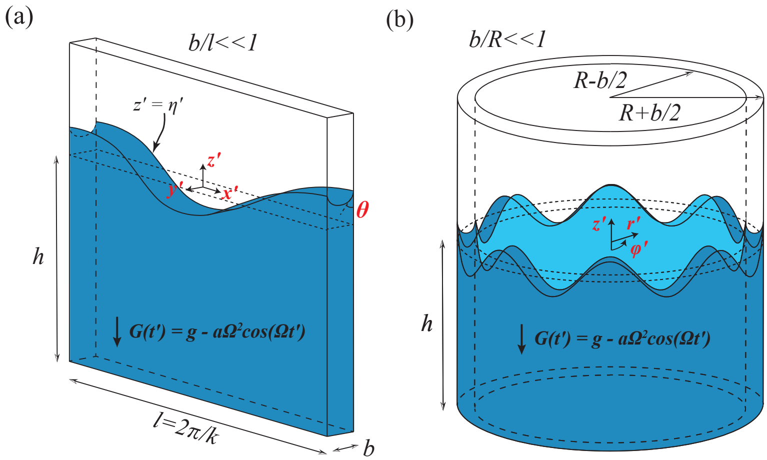


Figure 1: (a) Sketch of Faraday waves in a rectangular Hele-Shaw cell of width $b$ and length $l$ filled to a depth $h$ with a liquid. Here $b$ denotes the gap size of the Hele-Shaw cell, $l$ is the wavelength of a certain wave, such that $b/l \ll 1$, and $\theta$ is the dynamic contact angle of the liquid on the lateral walls. The vessel undergoes a vertical sinusoidal oscillation of amplitude $a$ and angular frequency $\Omega$. The free surface elevation is denoted by $\eta'(x')$. (b) Same as (a), but in an annular Hele-Shaw cell with internal and external radii, respectively, $R - b/2$ and $R + b/2$. Here, $b/R \ll 1$ and the free surface elevation is a function of the azimuthal coordinate $\varphi'$, i.e. $\eta'(\varphi')$.

## 2. Horizontally infinite Hele-Shaw cells

Let us begin by considering the case of a horizontally infinite Hele-Shaw cell of width $b$ filled to a depth $h$ with an incompressible fluid of density $\rho$, dynamic viscosity $\mu$ (kinematic viscosity $\nu = \mu/\rho$) and liquid-air surface tension $\gamma$ (see also sketch in figure 1(a)). The vessel undergoes a vertical sinusoidal oscillation of amplitude $a$ and angular frequency $\Omega$. In a frame of reference which moves with the oscillating container, the free liquid interface is flat and stationary for small forcing amplitudes, and the oscillation is equivalent to a temporally modulated gravitational acceleration, $G(t') = g - a\Omega^2 \cos \Omega t'$. The equation of motion for the fluid bulk are

$$\rho \left( \frac{\partial \mathbf{U}'}{\partial t'} + \mathbf{U}' \cdot \nabla' \mathbf{U}' \right) = -\nabla' P' + \mu \nabla'^2 \mathbf{U}' - \rho G(t) \, \mathbf{e}_z, \quad \nabla' \cdot \mathbf{U}' = 0. \tag{2.1}$$

Linearizing about the rest state $\mathbf{U}' = \mathbf{0}$ and $P'(z', t') = -\rho G(t') z'$, the equations for the perturbation velocity, $\mathbf{u}'(x', y', z', t') = \{u', v', w'\}^T$, and pressure, $p'(x', y', z', t')$, fields, associated with a certain perturbation's wavelength $l = 2\pi/k$ ($k$, wavenumber), read

$$\rho \frac{\partial \mathbf{u}'}{\partial t'} = -\nabla' p' + \mu \nabla'^2 \mathbf{u}', \quad \nabla' \cdot \mathbf{u}' = 0. \tag{2.2}$$

Assuming that $bk \ll 1$, then the velocity along the narrow $y'$-dimension $v' \ll u', w'$ and, by employing the Hele-Shaw approximation as in, for instance, Viola *et al.* (2017), one can simplify the linearised Navier-Stokes equations as follows:

$$\frac{\partial u'}{\partial x'} + \frac{\partial v'}{\partial y'} + \frac{\partial w'}{\partial z'} = 0, \tag{2.3$a$}$$

$$\rho \frac{\partial u'}{\partial t'} = -\frac{\partial p'}{\partial x'} + \mu \frac{\partial^2 u'}{\partial y'^2}, \quad \rho \frac{\partial w'}{\partial t'} = -\frac{\partial p'}{\partial z'} + \mu \frac{\partial^2 w'}{\partial y'^2}, \quad \frac{\partial p'}{\partial y'} = 0. \tag{2.3b}$$

Equations (2.3*a*)-(2.3*b*) are made dimensionless using $k^{-1}$ for the directions $x'$ and $z'$, and $b$ for $y'$. The forcing amplitude and frequency provide a scale $a\Omega$ for the in-plane $xz$-velocity components, whereas the continuity equation imposes the transverse component $v'$ to scale as $v' \sim bka\Omega \ll a\Omega \sim u'$, due to the strong confinement in the $y$-direction ($bk \ll 1$). With these choices, dimensionless spatial scales, velocity components and pressure write:

$$x = x'k, \;\; y = \frac{y'}{b}, \;\; z = z'k, \;\; u = \frac{u'}{a\Omega}, \;\; v = \frac{v'}{bka\Omega}, \;\; w = \frac{w'}{a\Omega}, \;\; p = \frac{kp'}{\rho a\Omega^2}, \;\; t = \Omega t'. \tag{2.4}$$

The first two equations in (2.3*b*) in non-dimensional form are

$$\frac{\partial u}{\partial t} = -\frac{\partial p}{\partial x} + \frac{\delta_{St}^2}{2}\frac{\partial^2 u}{\partial y^2}, \qquad \frac{\partial w}{\partial t} = -\frac{\partial p}{\partial z} + \frac{\delta_{St}^2}{2}\frac{\partial^2 w}{\partial y^2}, \tag{2.5}$$

where $\delta_{St} = \delta'_{St}/b$ and with $\delta'_{St} = \sqrt{2\nu/\Omega}$ denoting the thickness of the oscillating Stokes boundary layer. The ratio $\sqrt{2}/\delta_{St}$ is also commonly referred to as the Womersley number, $Wo = b\sqrt{\Omega/\nu}$ (Womersley 1955; San & Staples 2012).

### 2.1. *Floquet analysis of the gap-averaged equations*

Given its periodic nature, the stability of the base flow, represented by a time-periodic modulation of the hydrostatic pressure, can be investigated via Floquet analysis. We, therefore, introduce the following Floquet ansatz (Kumar & Tuckerman 1994)

$$\mathbf{u}\,(x,y,z,t) = e^{\mu_F t}\sum_{n=-\infty}^{+\infty}\tilde{\mathbf{u}}_n\,(x,y,z)\,e^{\mathrm{i}(n+\alpha/\Omega)t} = e^{\mu_F t}\sum_{n=-\infty}^{+\infty}\tilde{\mathbf{u}}_n\,(x,y,z)\,e^{\mathrm{i}\xi_n t}, \tag{2.6a}$$

$$p\,(x,z,t) = e^{\mu_F t}\sum_{n=-\infty}^{+\infty}\tilde{p}_n\,(x,z)\,e^{\mathrm{i}(n+\alpha/\Omega)t} = e^{\mu_F t}\sum_{n=-\infty}^{+\infty}\tilde{p}_n\,(x,z)\,e^{\mathrm{i}\xi_n t}, \tag{2.6b}$$

where $\mu_F$ is the real part of the non-dimensional Floquet exponent and represents the growth rate of the perturbation. We have rewritten $(n+\alpha/\Omega) = \xi_n$ to better explicit the parametric nature of the oscillation frequency of the wave response. In the following, we will focus on the condition for marginal stability (boundaries of the Faraday's tongues), which requires a growth rate $\mu_F = 0$. In addition, values of $\alpha = 0$ and $\Omega/2$ correspond, respectively, to harmonic and sub-harmonic parametric resonances (Kumar & Tuckerman 1994). This implies that $\xi_n$ is a parameter whose value is either $n$, for harmonics, or $n+1/2$, for sub-harmonics, with $n$ an integer $n = 0, 1, 2, \ldots$ specific to each Fourier component in (2.6*a*)-(2.6*b*).

By injecting the ansatzs (2.6*a*)-(2.6*b*) in (2.5), we find that each component of the Fourier series must satisfy

$$\forall n: \quad \mathrm{i}\xi_n\tilde{u}_n = -\frac{\partial \tilde{p}_n}{\partial x} + \frac{\delta_{St}^2}{2}\frac{\partial^2 \tilde{u}_n}{\partial y^2}, \qquad \mathrm{i}\xi_n\tilde{w}_n = -\frac{\partial \tilde{p}_n}{\partial z} + \frac{\delta_{St}^2}{2}\frac{\partial^2 \tilde{w}_n}{\partial y^2}, \tag{2.7}$$

which, along with the no-slip condition at $y = \pm 1/2$, correspond to a two-dimensional pulsatile Poiseuille flow with solution

$$\tilde{u}_n = \frac{\mathrm{i}}{\xi_n}\frac{\partial \tilde{p}_n}{\partial x}F_n\,(y), \qquad \tilde{w}_n = \frac{\mathrm{i}}{\xi_n}\frac{\partial \tilde{p}_n}{\partial z}F_n\,(y), \qquad F_n\,(y) = \left(1 - \frac{\cosh\left((1+\mathrm{i})\,y/\delta_n\right)}{\cosh\left((1+\mathrm{i})\,/2\delta_n\right)}\right), \tag{2.8}$$

and where $\delta_n = \delta_{St}/\sqrt{\xi_n}$, is a rescaled Stokes boundary layer thickness specific to the $n$th Fourier component. The function $F_n\,(y)$ is displayed in figure 2(b), which depicts how a decrease in the value of $\delta_n$ starting from large values corresponds to a progressive transition from a fully developed flow profile to a plug flow connected to thin boundary layers.

The gap-averaged velocity along the $y$-direction satisfies a Darcy-like equation,

$$\langle \tilde{\mathbf{u}}_n \rangle = \int_{-1/2}^{1/2} \tilde{\mathbf{u}}_n \,\mathrm{d}y = \frac{\mathrm{i}\beta_n}{\xi_n} \nabla \tilde{p}_n, \qquad \beta_n = 1 - \frac{2\delta_n}{1+\mathrm{i}} \tanh \frac{1+\mathrm{i}}{2\delta_n}. \tag{2.9}$$

To obtain a governing equation for the pressure $\tilde{p}_n$, we average the continuity equation and we impose the impermeability condition for the spanwise velocity, $v = 0$ at $y = \pm 1/2$,

$$\frac{\partial \langle \tilde{u}_n \rangle}{\partial x} + \underbrace{\int_{-1/2}^{1/2} \frac{\partial \tilde{v}_n}{\partial y} \,\mathrm{d}y}_{\tilde{v}_n(1/2) - \tilde{v}_n(-1/2) = 0} + \frac{\partial \langle \tilde{w}_n \rangle}{\partial z} = \nabla \cdot \langle \tilde{\mathbf{u}}_n \rangle = 0, \tag{2.10}$$

Since $\langle \tilde{\mathbf{u}}_n \rangle = \mathrm{i}\,(\beta_n/\xi_n)\,\nabla \tilde{p}_n$, the pressure field $\tilde{p}_n$ must obey the Laplace equation

$$\nabla^2 \tilde{p}_n = \frac{\partial^2 \tilde{p}_n}{\partial x^2} + \frac{\partial^2 \tilde{p}_n}{\partial z^2} = 0. \tag{2.11}$$

It is now useful to expand each Fourier component $\tilde{p}_n\,(x,z)$ in the infinite $x$-direction as $\sin x$ such that the $y$-average implies,

$$\tilde{p}_n\,(x,z) = \hat{p}_n\,(z) \sin x, \tag{2.12a}$$

$$\langle \tilde{u}_n \rangle = \frac{\mathrm{i}\beta_n}{\xi_n} \hat{p}_n \cos x = \hat{u}_n \cos x, \qquad \langle \tilde{w}_n \rangle = \frac{\mathrm{i}\beta_n}{\xi_n} \frac{\partial \hat{p}_n}{\partial z} \sin x = \hat{w}_n \sin x. \tag{2.12b}$$

Replacing (2.12*a*) in (2.11) leads to

$$\left( \frac{\partial^2}{\partial z^2} - 1 \right) \hat{p}_n = 0, \tag{2.13}$$

which admits the solution form

$$\hat{p}_n = c_1 \cosh z + c_2 \sinh z. \tag{2.14}$$

The presence of a solid bottom imposes that $\hat{w}_n = 0$ and, therefore, that $\partial \hat{p}_n / \partial z = 0$, at a non-dimensional fluid depth $z = -hk$, hence giving

$$\hat{p}_n = c_1 \left[ \cosh z + \tanh kh \sinh z \right]. \tag{2.15}$$

Let us now invoke the kinematic boundary condition linearised around a flat static interface

$$\frac{\partial \eta}{\partial t} = w. \tag{2.16}$$

Note that the free surface elevation, $\eta'\,(x', y', t')$, has been rescaled by the forcing amplitude $a$, i.e. $\eta'/a = \eta$, and represents the projection of the bottom of the transverse concave meniscus on the $xz$-plane of figure 1(a). Moreover, by recalling the Floquet ansatzs (2.6*a*)-(2.6*b*) (with $\mu_F = 0$), here specified for the interface, we get an equation for each Fourier component $n$,

$$\eta = \sum_{n=-\infty}^{+\infty} \tilde{\eta}_n e^{\mathrm{i}\xi_n t}. \tag{2.17}$$

Expanding $\tilde{\eta}_n$ in the $x$-direction as $\sin x$ and averaging in $y$, i.e. $\langle \tilde{\eta}_n \rangle = \hat{\eta}_n$, leads to

$$\forall n: \quad \mathrm{i}\xi_n \hat{\eta}_n = \hat{w}_n = \frac{\mathrm{i}\beta_n}{\xi_n} \left.\frac{\partial \hat{p}_n}{\partial z}\right|_{z=0} = \frac{\mathrm{i}\beta_n}{\xi_n} c_1 \tanh kh \quad \longrightarrow \quad c_1 = \frac{\xi_n^2}{\beta_n} \frac{\hat{\eta}_n}{\tanh kh}. \tag{2.18}$$

Lastly, we consider the dynamic equation (normal stress) linearised around a flat nominal interface and evaluated at $z'=0$,

$$-p'+\rho G(t')\eta'+2\mu\frac{\partial w'}{\partial z'}-\gamma\left(\frac{\partial^2\eta'}{\partial x'^2}+\frac{\partial^2\eta'}{\partial y'^2}\right)=0. \tag{2.19}$$

with the term in brackets in (2.19) that represents the first-order variation of the interface curvature. After turning to non-dimensional quantities using the scaling in (2.4), equations (2.19) reads

$$-\Omega^2 p+gk\eta-\frac{\gamma}{\rho}k\frac{\partial^2\eta}{\partial x^2}-\frac{\gamma}{\rho b^2}k\frac{\partial^2\eta}{\partial y^2}=\frac{a\Omega^2}{g}gk\,\eta\cos t, \tag{2.20}$$

where the viscous stress term has been neglected by analogy with Viola *et al.* (2017); Li *et al.* (2018*a*, 2019). Indeed, dimensional analysis suggests that such term scales as $\delta_{St}^2k^2b^2$ (with $kb\ll 1$), which is therefore negligible compared to the others as soon as $\delta_{St}$ is of order $\sim \mathrm{O}(1)$ or smaller.

The capillary force in the $x$-direction becomes important only at large enough wavenumbers, although the associated term can be retained in the analysis so as to retrieve the well-known dispersion relation (Saffman & Taylor 1958; Chuoke *et al.* 1959; McLean & Saffman 1981; Park & Homsy 1984; Schwartz 1986; Afkhami & Renardy 2013; Li *et al.* 2019). With the introduction of the Floquet ansatz (2.6*b*)-(2.17) and by recalling the $x$-expansion of the interface and pressure as $\sin x$, the averaged normal stress equation becomes

$$\forall n:\quad -\Omega^2\hat{p}_n+\left(1+\frac{\gamma}{\rho g}k^2\right)gk\hat{\eta}_n-\frac{\gamma}{\rho b^2}k\int_{-1/2}^{1/2}\frac{\partial^2\tilde{\eta}_n}{\partial y^2}\,\mathrm{d}y=\frac{a\Omega^2}{2g}gk\left(\hat{\eta}_{n-1}+\hat{\eta}_{n+1}\right). \tag{2.21}$$

where the decomposition $\cos\Omega t'=\left(e^{\mathrm{i}\Omega t'}+e^{-\mathrm{i}\Omega t'}\right)/2=\left(e^{\mathrm{i}t}+e^{-\mathrm{i}t}\right)/2$ has also been used to decompose the right-hand side into the $(n-1)$th and $(n+1)$th harmonics.

#### 2.1.1. *Treatment of the integral contact line term*

The treatment of the integral term hides several subtleties. Owing to the anti-symmetry of the first derivative of the interface at the two sidewalls, this term can be rewritten as

$$\int_{-1/2}^{1/2}\frac{\partial^2\tilde{\eta}_n}{\partial y^2}\,\mathrm{d}y=\left[\frac{\partial\tilde{\eta}_n}{\partial y}\right]_{y=-1/2}^{y=1/2}=2\left.\frac{\partial\tilde{\eta}_n}{\partial y}\right|_{y=1/2}. \tag{2.22}$$

Linking the interface position $\tilde{\eta}_n(y)$ to the vertical velocity $\tilde{w}_n(y)$ given by (2.8) through the kinematic equation (2.16), and then taking their y-derivative in $y=1/2$ to express $\left.\frac{\partial\tilde{\eta}_n}{\partial y}\right|_{y=1/2}$ seems the natural choice. However, this means assuming that the contact line remains pinned during the motion as $\tilde{w}_n$ satisfies the no-slip wall condition at $y=\pm 1/2$. Although the scenario of a pinned contact line dynamics (Benjamin & Scott 1979; Graham-Eagle 1983) is experimentally reproducible under controlled edge conditions (Henderson & Miles 1994; Howell *et al.* 2000; Bechhoefer *et al.* 1995; Shao *et al.* 2021*a*,*b*; Wilson *et al.* 2022), the most common experimental condition is that of a moving contact line (Benjamin & Ursell 1954; Henderson & Miles 1990; Batson *et al.* 2013; Li *et al.* 2015, 2016; Ward *et al.* 2019; Wilson *et al.* 2022; Li *et al.* 2019), which is not compatible with the no-slip condition satisfied by $\tilde{w}_n$. One natural option would be to relax this no-slip condition by introducing a small slip region in the vicinity of the contact line, within which the flow quickly adapts from a no-slip to a slip condition (Miles 1990; Ting & Perlin 1995). Accounting for this slip region, where the fluid speed relative to the solid is proportional to the viscous stress through a spatially varying slip length, is hardly compatible with the presently proposed depth-averaged modelling.

However, following Li *et al.* (2019); Hamraoui *et al.* (2000), it is possible to get inspiration from the contact line literature and relate the slope $\partial\tilde{\eta}_n/\partial y|_{y=1/2}$ to the gap-averaged contact line velocity $\langle\tilde{w}_n\rangle$ in the averaged sense, drawing a phenomenological analogy with the contact line law referred to as linear Hocking's model (Hocking 1987). To that purpose, the slope $\partial\tilde{\eta}_n/\partial y|_{y=1/2}$ is first related to the dynamic contact angle $\theta(t)$ through the geometrical relation

$$\left.\frac{\partial\eta'}{\partial y'}\right|_{y'=b/2} = \cot\theta. \tag{2.23}$$

Assuming the static interface to be flat means taking the static contact angle $\theta_s$ equal to $\pi/2$. Linearization of (2.23) around $\theta_s = \pi/2$ and substitution of the Floquet ansatz lead, in non-dimensional form, to

$$\forall n:\ \left.\frac{\partial\tilde{\eta}_n}{\partial y}\right|_{y=1/2} = -\frac{b}{a}\theta_n, \tag{2.24}$$

with $\theta_n$ representing a small angle variation around $\theta_s$ associated with $n$th harmonic. Defining $\langle Ca\rangle = (\mu/\gamma)\langle w'\rangle$, we prescribe

$$\forall n:\ \theta_n = \frac{M}{\gamma}a\Omega\langle\tilde{w}_n\rangle = a\frac{M}{\gamma}\mathrm{i}\left(\xi_n\Omega\right)\hat{\eta}_n. \tag{2.25}$$

The friction coefficient $M$, sometimes referred to as mobility parameter $M$ (Xia & Steen 2018), is here not interpreted in the framework of molecular kinetics theory (Voinov 1976; Hocking 1987; Blake 1993, 2006; Johansson & Hess 2018) but rather viewed as a constant phenomenological parameter that defines the energy dissipation rate per unit length of the contact line and, as in Li *et al.* (2019), we use the values proposed by Hamraoui *et al.* (2000).

In Hocking's model (Hocking 1987), adopting a value of $M = 0$ naturally means considering a contact line freely oscillating with a constant slope, while taking $M = +\infty$ simulates the case of a pinned contact line with fixed elevation. In contrast, in the present Hele-Shaw framework, the Capillary number can only be defined in terms of averaged interface velocity, so one cannot distinguish the contact line motion from the averaged interface evolution. As a result, the averaged model overlooks the free-to-pinned transition described by Hocking (1987) at large $M$, and somewhat paradoxically, the pinned regime cannot be described with this law.

### 2.1.2. *Modified damping coefficient*

Equations (2.15) and (2.18) are finally used to express the dynamic equation as a function of the non-dimensional averaged interface only,

$$-\frac{\left(\xi_n\Omega\right)^2}{\beta_n}\hat{\eta}_n + \mathrm{i}\left(\xi_n\Omega\right)\frac{2M}{\rho b}k\tanh kh\hat{\eta}_n + (1+\Gamma)\,gk\tanh kh\,\hat{\eta}_n = \frac{gk\tanh kh}{2}f\left(\hat{\eta}_{n-1}+\hat{\eta}_{n+1}\right), \tag{2.26}$$

with the auxiliary variables $f = a\Omega^2/g$ and $\Gamma = \gamma k^2/\rho g$, such that $(1+\Gamma)\,gk\tanh kh = \omega_0^2$, the well-known dispersion relation for capillary-gravity waves (Lamb 1993).

As in the present form, the interpretation of coefficient $\beta_n$ does not appear straightforward, it is useful to define the damping coefficients

$$\sigma_n = \sigma_{BL} + \sigma_{CL}, \quad \sigma_{BL} = \chi_n\frac{\nu}{b^2}, \quad \sigma_{CL} = \frac{2M}{\rho b}k\tanh kh, \tag{2.27a}$$

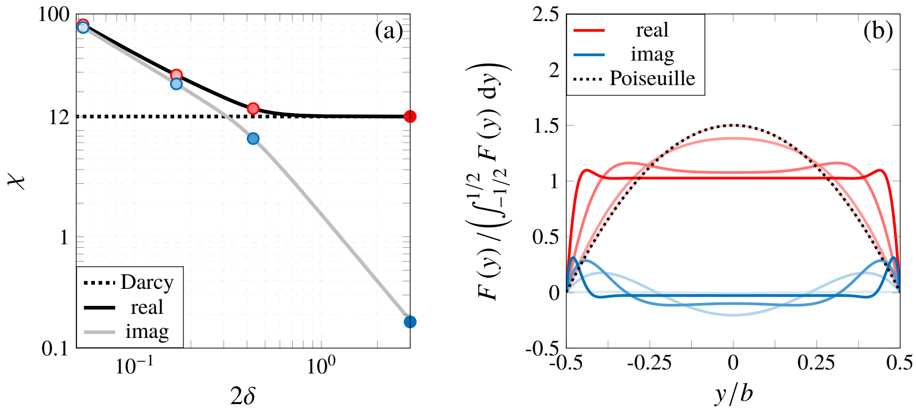


Figure 2: (a) Real and imaginary parts of the complex auxiliary coefficient $\chi = \chi_r + \mathrm{i}\chi_i$ versus twice the non-dimensional Stokes boundary layer thickness $\delta$. The horizontal black dotted line indicates the constant value 12 given by the Darcy approximation. (b) Normalised profile $F(y)$ (Womersley profile) for different $\delta = b^{-1}\sqrt{2\nu/\xi\Omega}$, whose values are specified by the filled circles in (a) with matching colours. The Poiseuille profile is also reported for completeness. In drawing these figures, we let the oscillation frequency of the wave, $\xi\Omega$, free to assume any value, but we recall that the parameter $\xi$ can only assume discrete values, and so do $\chi$ and $F(y)$.

where $\chi_n$ is used to help rewriting $\frac{1}{\beta_n} = 1 - \mathrm{i}\frac{\delta_n^2}{2}\chi_n$,

$$\chi_n = \mathrm{i}\frac{2}{\delta_n^2}\left(\frac{1-\beta_n}{\beta_n}\right) = 12\left[\frac{\mathrm{i}}{6\delta_n^2}\left(\frac{\frac{2\delta_n}{1+\mathrm{i}}\tanh\frac{1+\mathrm{i}}{2\delta_n}}{1-\frac{2\delta_n}{1+\mathrm{i}}\tanh\frac{1+\mathrm{i}}{2\delta_n}}\right)\right]. \tag{2.27b}$$

These auxiliary definitions allows one to express (2.26) as

$$-(\xi_n\Omega)^2\,\hat{\eta}_n + \mathrm{i}\,(\xi_n\Omega)\,\sigma_n\hat{\eta}_n + \omega_0^2\hat{\eta}_n = \frac{\omega_0^2}{2\,(1+\Gamma)}\,f\,[\hat{\eta}_{n+1} + \hat{\eta}_{n-1})]. \tag{2.28}$$

or, equivalently,

$$\frac{2\,(1+\Gamma)}{\omega_0^2}\left[-(n\Omega+\alpha)^2 + \mathrm{i}\,(n\Omega+\alpha)\,\sigma_n + \omega_0^2\right]\hat{\eta}_n = f\,[\hat{\eta}_{n+1} + \hat{\eta}_{n-1}]\,. \tag{2.29}$$

Subscripts $BL$ and $CL$ in (2.27$a$) denote, respectively, the boundary layers and contact line contributions to the total damping coefficient $\sigma_n$.

### 2.1.3. *Results*

At the end of this mathematical derivation, a useful result is the modified damping coefficient $\sigma_n$. Since the boundary layer contribution, $\sigma_{BL}$ depends on the $n$th Fourier component, the overall damping, $\sigma_n$, is mode dependent and its value is different for each specific $n$th parametric resonant tongue considered. This starkly contrasts with the standard Darcy approximation, where $\sigma_{BL}$ is the same for each resonance and amounts to $12\nu/b^2$. In our model, the case of $\alpha = 0$ with $n = 0$ constitutes a peculiar case, as $\xi_n = \xi_0 = 0$ and $\delta_0 \to +\infty$. In such a situation, $F_0(y)$ tends to the steady Poiseuille profile so that we take $\chi_0 = 12$.

Similarly to Kumar & Tuckerman (1994), equation (2.29) is rewritten as

$$A_n\hat{\eta}_n = f\,[\hat{\eta}_{n+1} + \hat{\eta}_{n-1}]\,, \tag{2.30}$$

with

$$A_n = \frac{2\,(1+\Gamma)}{\omega_0^2}\left(-\,(n\Omega+\alpha)^2 + \mathrm{i}\,(n\Omega+\alpha)\,\sigma_n + \omega_0^2\right) = A_n^r + \mathrm{i}A_n^i \in \mathbb{C} \tag{2.31}$$

The non-dimensional amplitude of the external forcing, $f = a\Omega^2/g$ appears linearly, therefore (2.30) can be considered to be a generalized eigenvalue problem

$$\mathbf{A}\hat{\eta} = f\mathbf{B}\hat{\eta}, \tag{2.32}$$

with eigenvalues $f$ and eigenvectors whose components are the real and imaginary parts of $\hat{\eta}_n$. See Kumar & Tuckerman (1994) for the structure of matrices $\mathbf{A}$ and $\mathbf{B}$.

For one frequency forcing we use a truncation number $N = 10$, which produces $2\,(N+1)\times 2\,(N+1) = 22\times 22$ matrices. Eigen-problem (2.32) is then solved in Matlab using the built-in function *eigs* and selecting several smallest, real positive values of $f$. For a fixed forcing frequency $\Omega$ and wavenumber $k$, the eigenvalue with the smallest real part will define the instability threshold. Further details about the numerical convergence as the truncation number $N$ varies are given in Appendix A.

Figure 3 shows the results of this procedure for one of the configurations considered by Li *et al.* (2019) and neglecting the dissipation associated with the contact line motion, i.e. $M = 0$. In each panel, associated with a fixed forcing frequency, the black regions correspond to the unstable Faraday tongues computed using $\sigma_{BL} = 12\nu/b^2$ as given by Darcy's approximation, whereas the red regions are the unstable tongues computed with the modified $\sigma_{BL} = \chi_n\nu/b^2$. At a forcing frequency 4 Hz, the first sub-harmonic tongues computed using the two models essentially overlap. Yet, successive resonances display an increasing departure from Darcy's model due to the newly introduced complex coefficient $\sigma_n$. Particularly, the real part of $\chi_n$ is responsible for the higher onset acceleration, while the imaginary part is expected to act as a detuning term, which shifts the resonant wavenumbers $k$.

### 2.2. *Asymptotic approximations*

The main result of this analysis consists in the derivation of the modified damping coefficient $\sigma_n = \sigma_{n,r} + \mathrm{i}\sigma_{n,i}$ associated with each parametric resonance. Aiming at better elucidating how this modified complex damping influences the stability properties of the system, we would like to derive in this section an asymptotic approximation, valid in the limit of small forcing amplitudes, damping and detuning, of the first sub-harmonic (SH1) and harmonic (H1) Faraday tongues.

Unfortunately, the dependence of $\sigma_n$ on the parametric resonance considered and, more specifically, on the $n$th Fourier component, does not allow one to directly convert the governing equations (2.28), expressed in a discrete frequency domain, back into the continuous temporal domain. By keeping this in mind, we can still imagine fixing the value of $\sigma_n$ to that corresponding to the parametric resonance of interest, e.g. $\sigma_0$ (with $n = 0$ and $\xi_0\Omega = \Omega/2$) for SH1 or $\sigma_1$ (with $n = 1$ and $\xi_1\Omega = \Omega$) for H1. By considering then that for the SH1 and H1 tongues, the system responds in time as $\exp(\mathrm{i}\Omega t/2)$ and $\exp(\mathrm{i}\Omega t)$, respectively, we can recast, for these two specific cases, equations (2.28) into a damped Mathieu equation (Benjamin & Ursell 1954; Kumar & Tuckerman 1994; Müller *et al.* 1997)

$$\frac{\partial^2\hat{\eta}}{\partial t'^2} + \hat{\sigma}_n\frac{\partial\hat{\eta}}{\partial t'} + \omega_0^2\left(1 - \frac{f}{1+\Gamma}\cos\Omega t'\right)\hat{\eta} = 0. \tag{2.33}$$

with either $\hat{\sigma}_n = \sigma_0$ (SH1) or $\hat{\sigma}_n = \sigma_1$ (H1) and where one can recognize that $-\,(\xi_n\Omega)^2\,\hat{\eta} \leftrightarrow \partial^2\hat{\eta}/\partial t'^2$ and $\mathrm{i}\,(\xi_n\Omega)\,\hat{\eta} \leftrightarrow \partial\hat{\eta}/\partial t'$. Asymptotic approximations can be then computed by

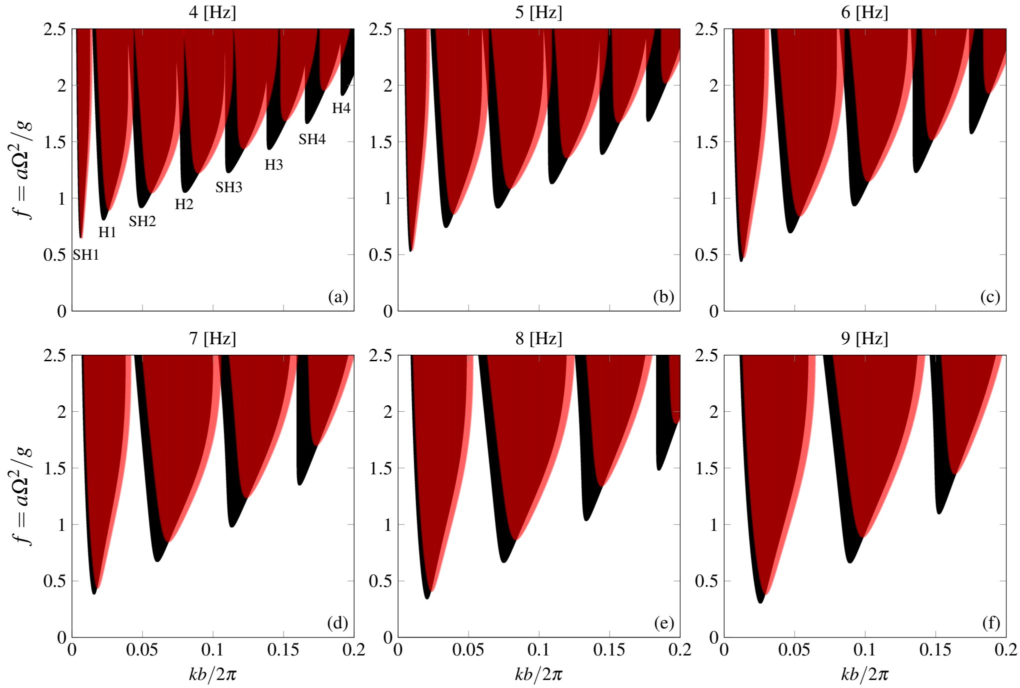


Figure 3: Faraday tongues computed via Floquet analysis at different fixed driving frequencies (reported on the top of each panel). Black regions correspond to the unstable Faraday tongues computed using $\sigma_{BL} = 12\nu/b^2$ as in the standard Darcy approximation, whereas red regions are the unstable tongues computed with the present modified $\sigma_{BL} = \chi_n \nu/b^2$. For this example, we consider ethanol 99.7% (see table 1) in a Hele-Shaw cell of gap size $b = 2$ mm filled to a depth $h = 60$ mm. $f$ denotes the non-dimensional forcing acceleration, $f = a\Omega^2/g$, with dimensional forcing amplitude $a$ and angular frequency $\Omega$. For plotting, we define a small scale-separation parameter $\epsilon = kb/2\pi$ and arbitrarily set its maximum acceptable value to 0.2. Contact line dissipation is not included, i.e. $M = \sigma_{CL} = 0$. SH stands for sub-harmonic, whereas $H$ stands for harmonic.

expanding asymptotically the interface as $\hat{\eta} = \hat{\eta}_0 + \epsilon\hat{\eta}_1 + \epsilon^2\hat{\eta}_2 + \ldots$, with $\epsilon$ a small parameter $\ll 1$.

### 2.2.1. *First sub-harmonic tongue*

As anticipated above, when looking at the first or fundamental sub-harmonic tongue (SH1), one should take $\hat{\sigma}_n \longrightarrow \sigma_0$ (with $\xi_0\Omega = \Omega/2$), which is assumed small of order $\epsilon$. The forcing amplitude $f$ is also assumed of order $\epsilon$. Furthermore, a small detuning $\sim \epsilon$, such that $\Omega = 2\omega_0 + \epsilon\lambda$, is also considered, and, in the spirit of the multiple timescale analysis, a slow time scale $\tau' = \epsilon t'$ (Nayfeh 2008) is introduced. At leading order, the solution reads $\hat{\eta}_0 = A(\tau')e^{\mathrm{i}\omega_0 t'} + c.c.$, with $c.c.$ denoting the complex conjugate part. At the second order in $\epsilon$, the imposition of a solvability condition necessary to avoid secular terms prescribes the amplitude $B(\tau') = A(\tau')e^{-\mathrm{i}\lambda\tau'/2}$ to obey the following amplitude equation

$$\frac{dB}{d\tau'} = -\frac{\sigma_0}{2}B - \mathrm{i}\frac{\lambda}{2}B - \mathrm{i}\frac{\omega_0}{4\,(1+\Gamma)}f\overline{B}. \tag{2.34}$$

Turning to polar coordinates, i.e. $B = |B|e^{\mathrm{i}\Phi}$, keeping in mind that $\sigma_0 = \sigma_{0,r} + \mathrm{i}\sigma_{0,i}$ and looking for stationary solutions with $|B| \neq 0$ (we skip the straightforward mathematical steps), one ends up with the following approximation for the marginal stability boundaries

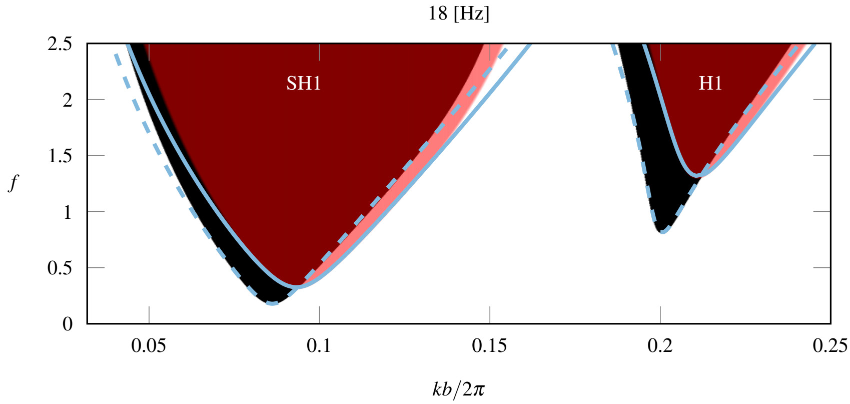


Figure 4: First sub-harmonic and harmonic Faraday tongues at a driving frquency $1/T = 18\,\mathrm{Hz}$ ($T$: forcing period) for the same configuration of figure 3. Black and red regions show unstable tongues computed via Floquet analysis by using, respectively, $\sigma_{BL} = 12\nu/b^2$ and the modified $\sigma_{BL} = \chi_1\nu/b^2$ from the present model. Dashed and solid light-blue lines correspond to the asymptotic approximations according to (2.35)-(2.38).

associated with the first sub-harmonic Faraday tongue

$$\left(\frac{\Omega + \sigma_{0,i}}{2\omega_0} - 1\right) = \pm\frac{1}{4\,(1+\Gamma)}\sqrt{f^2 - \frac{4\sigma_{0,r}^2\,(1+\Gamma)^2}{\omega_0^2}}, \tag{2.35}$$

whose onset acceleration value, min $f_{1_{SH}}$, for a fixed driving frequency $\Omega/2\pi$, amounts to

$$\min f_{SH1} = 2\sigma_{0,r}\sqrt{\frac{1+\Gamma}{gk\tanh kh}} \approx 2\sigma_{0,r}\sqrt{\frac{1}{g}\left(\frac{1}{k} + \frac{\gamma}{\rho g}k\right)}, \tag{2.36}$$

Note that the final approximation on the right-hand-side of (2.36) only holds if $kh \gg 1$, so that $\tanh kh \approx 1$ (deep water regime). Given that $\chi_{0,r} > 12$ and $\chi_{0,i} > 0$ always, the asymptotic approximation (2.36), in its range of validity, suggests that Darcy's model underestimates the sub-harmonic stability threshold. Moreover, from (2.35), the critical wavenumber $k$, associated with min $f_{SH1}$, would correspond to that prescribed by the Darcy approximation but at an effective forcing frequency $\Omega + \sigma_{0,i} = 2\omega_0$ instead of at $\Omega = 2\omega_0$. This explains why the modified tongues appear to be shifted towards higher wavenumbers. These observations are well visible in figure 4.

### 2.2.2. *First harmonic tongue*

By analogy with §2.2.1, an analytical approximation of the first harmonic tongue (H1) can be provided. In the same spirit of Rajchenbach & Clamond (2015), we adapt the asymptotic scaling such that $f$ is still of order $\epsilon$, but $\tau' = \epsilon^2 t'$, $\hat{\sigma}_n = \sigma_1 \sim \epsilon^2$ (with $\xi_1\Omega = \Omega$) and $\Omega = \omega_0 + \epsilon^2\lambda$. Pursuing the expansion up to $\epsilon^2$-order, with $\hat{\eta}_0 = A(\tau')e^{\mathrm{i}\omega_0 t'} + c.c.$ and $B(\tau') = A(\tau')e^{-\mathrm{i}\lambda\tau'}$, will provide the amplitude equation

$$\frac{dB}{d\tau'} = -\frac{\sigma_1}{2}B - \mathrm{i}\lambda B - \mathrm{i}\frac{\omega_0}{8\,(1+\Gamma)^2}f^2\overline{B} + \mathrm{i}\frac{\omega_0}{12\,(1+\Gamma)^2}f^2 B. \tag{2.37}$$

| Liquid | $\mu$ [mPa s] | $\rho$ [kg/m$^3$] | $\gamma$ [N/m] | $M$ [Pa s] |
|---|---|---|---|---|
| ethanol 99.7% | 1.096 | 785 | 0.0218 | 0.04 |
| ethanol 70.0% | 2.159 | 835 | 0.0234 | 0.0485 |
| ethanol 50.0% | 2.362 | 926 | 0.0296 | 0.07 |

Table 1: Characteristic fluid parameters for the three ethanol-water mixtures considered in this study. Data for the pure ethanol and ethanol-water mixture (50%) are taken from Li *et al.* (2019). The value of the friction parameter $M$ for ethanol-70% is fitted from the experimental measurements reported in §4, but lies well within the range of values used by Li *et al.* (2019) and agrees with the linear trend displayed in figure 5 of Hamraoui *et al.* (2000).

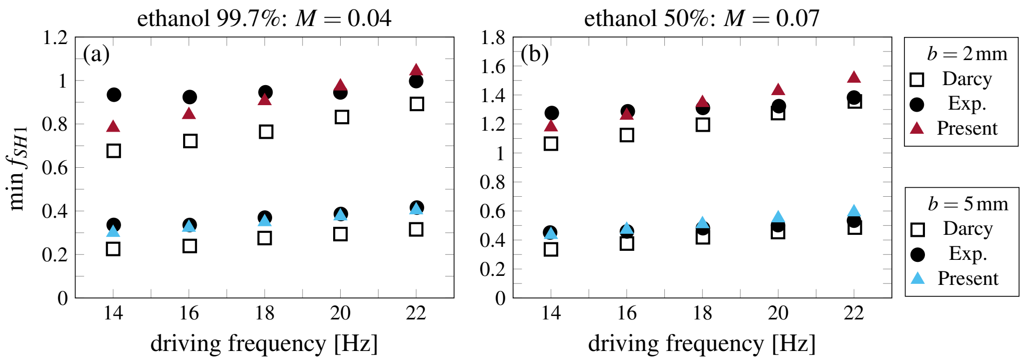


Figure 5: Sub-harmonic instability onset, min $f$, versus driving frequency, $1/T$ ($T$: forcing period). Comparison between theoretical data (empty squares: standard Darcy model, $\sigma_{BL} = 12\nu/b^2$; coloured triangles: present model, $\sigma_{BL} = \chi_n \nu/b^2$) and experimental measurements by Li *et al.* (2019). The values of the mobility parameter $M$ here employed are reported in the figure.

The approximation for the marginal stability boundaries derived from (2.37) takes the form

$$\left(\frac{\Omega + \sigma_{1,i}/2}{\omega_0} - 1\right) = \frac{f^2}{12\,(1+\Gamma)^2} \pm \frac{1}{8\,(1+\Gamma)^2}\sqrt{f^4 - \left(\frac{4\sigma_{1,r}\,(1+\Gamma)^2}{\omega_0}\right)^2} \tag{2.38}$$

with a minimum onset acceleration, min $f_{1_H}$

$$\min f_H = 2\sqrt{\sigma_{1,r}}\left(\frac{(1+\Gamma)^3}{gk\tanh kh}\right)^{1/4} \approx 2\sqrt{\sigma_{1,r}}\,\frac{1}{g^{1/4}}\left(\frac{1}{k^{1/3}} + \frac{\gamma}{\rho g}k^{5/3}\right)^{3/4}, \tag{2.39}$$

and where, as before, the final approximation on the right-hand side is only valid in the deep water regime. Similarly to the sub-harmonic case, the critical wavenumber $k$ corresponds to that prescribed by the Darcy approximation but at an effective forcing frequency $\Omega + \sigma_{1,i}/2 = \omega_0$ instead of at $\Omega = \omega_0$ and the onset acceleration is larger than that predicted from the Darcy approximation (as $\chi_{1,r} > 12$).

### 2.3. *Comparison with experiments by Li* et al. *(2019)*

Results presented so far were produced by assuming the absence of contact line dissipation, i.e. coefficient $M$ was set to $M = 0$ so that $\sigma_{CL} = 0$. In this section, we reintroduce such a dissipative contribution and we compare our theoretical predictions with a set of experimental measurements reported by Li *et al.* (2019), using the values they have proposed for M. This comparison, shown in figure 5, is outlined in terms of non-dimensional minimum onset acceleration, $\min f = \min f_{SH1}$, versus driving frequency. These authors performed experiments in two different Hele-Shaw cells of length $l = 300\,\mathrm{mm}$, fluid depth $h = 60\,\mathrm{mm}$ and gap-size $b = 2\,\mathrm{mm}$ or $b = 5\,\mathrm{mm}$. Two fluids, whose properties are reported in table 1, were used: ethanol 99.7% and ethanol 50%. The empty squares in figure 5 are computed via Floquet stability analysis (2.32) using the Darcy approximation for $\sigma_{BL} = 12\nu/b^2$ and correspond to the theoretical prediction by Li *et al.* (2019), while the coloured triangles are computed using the present theory, with the corrected $\sigma_{BL} = \chi_n\nu/b^2$. Although the trend is approximately the same, the Darcy approximation underestimates the onset acceleration with respect to the present model, which overall compares better with the experimental measurements (black-filled circles). Some disagreement still exists, especially at smaller cell gaps, i.e. $b = 2\,\mathrm{mm}$, where surface tension effects are even more prominent. This is likely attributable to an imperfect phenomenological contact line model (Bongarzone *et al.* 2021, 2022*b*), whose definition falls beyond the scope of this work. Yet, this comparison shows how the modifications introduced by the present model contribute to closing the gap between theoretical Faraday onset estimates and these experiments.

## 3. The case of thin annuli

We now consider the case of a thin annular container, whose nominal radius is $R$ and the actual inner and outer radii are $R-b/2$ and $R+b/2$, respectively (see the sketch in figure 1(b)). In the limit of $b/R \ll 1$, the wall curvature is negligible and the annular container can be considered a Hele-Shaw cell. The following change of variable for the radial coordinate, $r' = R + y' = R\,(1 + y'/R)$ with $y' \in [-b/2, b/2]$, will be useful in the rest of the analysis. As in §2, we first linearise around the rest state. Successively, we introduce the following non-dimensional quantities,

$$r = \frac{r'}{R},\quad y = \frac{y'}{b},\quad z = \frac{z'}{R},\quad u = \frac{u'_\varphi}{a\Omega},\quad v = \frac{u'_r}{a\Omega\,(b/R)},\quad w = \frac{u'_z}{a\Omega},\quad p = \frac{p'}{\rho R a \Omega^2}. \tag{3.1}$$

It follows that, at leading order, $r = 1 + yb/R \sim 1 \longrightarrow 1/r = 1/(1 + yb/R) \sim 1$ but $\partial/\partial_r = (R/b)\,\partial/\partial_y \sim (b/R)^{-1} \gg 1$. With this scaling and introducing the Floquet ansatzs (2.6*a*)-(2.6*b*), one obtains the following simplified governing equations,

$$\frac{\partial \tilde{u}_n}{\partial \varphi} + \frac{\partial \tilde{v}_n}{\partial y} + \frac{\partial \tilde{w}_n}{\partial z} = 0, \tag{3.2a}$$

$$\mathrm{i}\tilde{u}_n = -\frac{1}{\xi_n}\frac{\partial \tilde{p}_n}{\partial \varphi} + \frac{\delta_n^2}{2}\frac{\partial^2 \tilde{u}_n}{\partial y^2},\quad \mathrm{i}\tilde{w}_n = -\frac{1}{\xi_n}\frac{\partial \tilde{p}_n}{\partial z} + \frac{\delta_n^2}{2}\frac{\partial^2 \tilde{w}_n}{\partial y^2}\quad \text{or}\quad \tilde{\mathbf{u}}_n = \frac{\mathrm{i}}{\xi_n}\nabla \tilde{p}_n F_n(y), \tag{3.2b}$$

which are fully equivalent to those for the case of conventional rectangular cells if the transformation $\varphi \longrightarrow x$ is introduced. Averaging the continuity equation with the imposition of the no-penetration condition at $y = \mp 1/2$, $v\,(\mp 1/2)$, eventually leads to

$$\nabla^2 \tilde{p}_n = \frac{\partial^2 \tilde{p}_n}{\partial z^2} + \frac{\partial^2 \tilde{p}_n}{\partial \varphi^2}, \tag{3.3}$$

identically to (2.11). Expanding $\tilde{p}_n$ in the azimuthal direction as $\tilde{p}_n = \hat{p}_n \sin m\varphi$, with $m$ the azimuthal wavenumber, provides

$$\left(\frac{\partial^2}{\partial z^2} - m^2\right)\hat{p}_n = 0 \quad \longrightarrow \quad \hat{p}_n = c_1 \cosh mz + c_2 \sinh mz, \tag{3.4}$$

and the no-penetration condition at the solid bottom located at $z = -h/R$, $\hat{w}_n = \partial_z \hat{p}_n = 0$, prescribes

$$\hat{p}_n = c_1 \left(\cosh mz + \tanh mh/R \sinh mz\right). \tag{3.5}$$

Although so far the theory for the rectangular and the annular cases is the same, here it is crucial to observe that the axisymmetric container geometry translates into a periodicity condition:

$$\sin(-m\pi) = \sin(m\pi) \quad \longrightarrow \quad \sin m\pi = 0, \tag{3.6}$$

which always imposes the azimuthal wavenumber to be an integer. In other words, in contradistinction with the case of §2, where the absence of lateral wall ideally allows for any wavenumber $k$, here we have $m = 0, 1, 2, 3, \ldots \in \mathbb{N}$.

By repeating the calculations outlined in §2, one ends up with the same equation (2.29) (and subsequent (2.30)-(2.32)), but where $\omega_0$ obeys to the *quantized* dispersion relation

$$\omega_0^2 = \left(\frac{g}{R}m + \frac{\gamma}{\rho R^3}m^3\right)\tanh m\frac{h}{R} = (1+\Gamma)\frac{g}{R}m \tanh m\frac{h}{R}. \tag{3.7}$$

with $\Gamma = \gamma m^2/\rho g R^2$. In this context, a representation of Faraday's tongues in the forcing frequency-amplitude plane appears most natural, as each parametric tongue will correspond to a fixed wavenumber $m$. Consequently, instead of fixing $\Omega$ and varying the wavenumber, here we solve (2.32) by fixing $m$ and varying $\Omega$.

### 3.1. *Floquet analysis and asymptotic approximation*

The results from this procedure are reported in figure 6, where, as in figure 3, the black regions correspond to the unstable tongues obtained according to the standard gap-averaged Darcy model, while the red ones are computed using the present theory with the corrected gap-averaged $\sigma_{BL} = \chi_n \nu/b^2$. The regions with the lowest thresholds in each panel are sub-harmonic tongues associated with modes from $m = 1$ to 14. In figure 6(a), no contact line model is included, i.e. $M = 0$, whereas in (b) a mobility parameter $M = 0.0485$ is accounted for. Panel (b) shows how the additional contact line dissipation, introduced by $\sigma_{CL} \propto m$ (see equation (2.27*a*)), dictates the linear-like trend followed by the minimum onset acceleration at larger azimuthal wavenumbers. The use of this specific value for $M$ will be clarified in the next section when comparing the theory with dedicated experiments, but a thorough sensitivity analysis to variations of $M$ is carried out in Appendix B.

In general, the present model gives a higher instability threshold, consistent with the results reported in the previous section. However, the tongues are here shifted to the left.

The asymptotic approximation for the sub-harmonic onset acceleration, adapted to this case from (2.35) yields:

$$f_{SH1} = 2\sqrt{(1+\Gamma)\frac{\sigma_{0,r}^2}{(g/R)\,m\tanh mh/R} + 4(1+\Gamma)^2\left(\frac{\Omega+\sigma_{0,i}}{2\omega_0} - 1\right)^2}, \tag{3.8}$$

with

$$\min f_{SH1} = 2\sigma_{0,r}\frac{1+\Gamma}{\omega_0} = 2\sigma_{0,r}\sqrt{\frac{1+\Gamma}{(g/R)\,m\tanh mh/R}} \approx 2\sigma_{0,r}\sqrt{\frac{R}{g}\left(\frac{1}{m} + \frac{\gamma}{\rho g R^2}m\right)}, \tag{3.9}$$

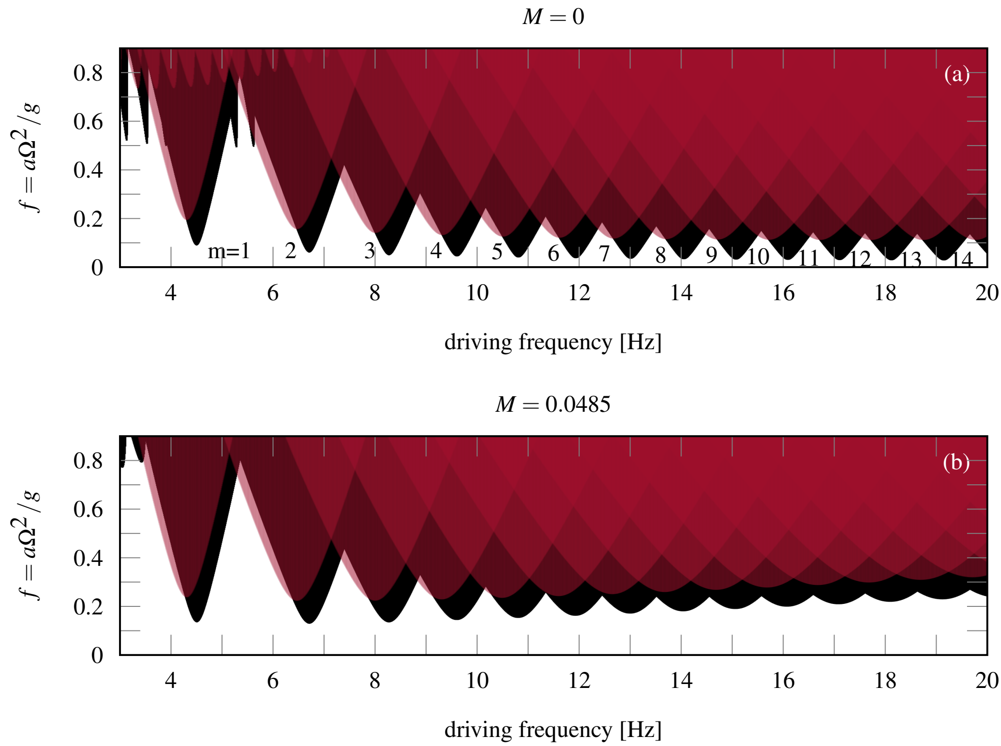


Figure 6: Faraday tongues computed via Floquet analysis (2.32) at different fixed azimuthal wavenumber $m$ and varying the driving frequency, $\Omega/2/\pi$. Black regions correspond to the unstable Faraday tongues computed using $\sigma_{BL} = 12\nu/b^2$, whereas red regions are the unstable tongues computed with the present modified $\sigma_{BL} = \chi_n \nu/b^2$. The fluid parameters used here correspond to those given in table 1 for ethanol 70%. The gap-size is set to $b = 7$ mm, the fluid depth to $h = 65$ mm and the nominal radius to $R = 44$ mm. Contact line dissipation is included in (b) and (d) by accounting for a mobility coefficient $M = 0.0485$. The regions with the lowest thresholds in each panel are sub-harmonic tongues associated with modes from $m = 1$ to 14.

helps us in rationalising the influence of the modified complex damping coefficient.

This apparent opposite correction is a natural consequence of the different representations: varying wavenumber at a fixed forcing frequency (as in figure 3) versus varying forcing frequency at a fixed wavenumber (figure 6). Such a behaviour is clarified by the asymptotic relation (3.8) and, particularly by the term $\left(\frac{\Omega+\sigma_{0,i}}{2\omega_0} - 1\right)$. In §2, the analysis is based on a fixed forcing frequency, while the wavenumber $k$ and, hence, the natural frequency $\omega_0$, are free to vary. The first sub-harmonic Faraday tongue occurs when $\Omega + \sigma_{0,i} \approx 2\omega_0$. Since $\Omega$ is fixed and $\sigma_{0,i} > 0$, $\Omega + \sigma_{0,i} > \Omega$ such that $\omega_0$ and therefore $k$ have to increase in order to satisfy the relation. On the other hand, if the wavenumber $m$ and, hence, $\omega_0$ are fixed as in this section, then $2\omega_0 - \sigma_{0,i} < 2\omega_0$ and the forcing frequency around which the sub-harmonic resonance is centred, decreases of a contribution $\sigma_{0,i}$, which introduces a frequency detuning responsible for the negative frequency shift displayed in figure 6.

### 3.2. *Discussion on the system's spatial quantization*

The frequency-dependence of the damping coefficient $\sigma_n$ associated with each Faraday's tongue is one of the first aspects that needs to be better discussed. In the case of horizontally infinite cells, the most natural description for investigating the system's stability properties is in the $(k, f)$ plane for a fixed forcing angular frequency $\Omega$ (Kumar & Tuckerman 1994). According to our model, the oscillating system's response occurring within each tongue is characterised by a Stokes boundary layer thickness $\delta_n = \sqrt{2\nu/(n\Omega+\alpha)}/b$. For instance, let us consider sub-harmonic resonances with $\alpha = \Omega/2$. As $\Omega$ is fixed (see any sub-panel of figure 3), each unstable region sees a constant $\delta_n$ (with $n = 0, 1, 2, \ldots$) and hence a constant damping $\sigma_n$.

On the other hand, in the case of quantised wavenumber as for the annular cell of §3, the most suitable description is in the driving frequency-driving amplitude plane at fixed wavenumber $m$ (see figure 6) (Batson *et al.* 2013). In this description, each sub-harmonic ($\alpha = \Omega/2$) or harmonic ($\alpha = \Omega$) $n$th tongue associated with a wavenumber $m$, sees a $\delta_n$, and thus a $\sigma_n$, changing with $\Omega$ along the tongue itself.

## 4. Experiments

In a real lab-scale experiment, the horizontal size of rectangular cells is never infinite due to the presence of lateral walls in the elongated direction. In such a case, however, the solution form (2.9) prevents the no-slip condition for the in-plane $xz$-velocity components to be imposed (Viola *et al.* 2017). This always translates into a theoretical underestimation of the overall damping of the system in rectangular Hele-Shaw cells, although the sidewall contribution is expected to be negligible for sufficiently long cells.

On the other hand, the case of a thin annulus, by naturally filtering out this extra dissipation owing to the periodicity condition, offers a prototype configuration that can potentially allow one to quantify better the correction introduced by the present gap-averaged model when compared to dedicated experiments.

### 4.1. *Setup*

The experimental apparatus, shown in figure 7, consists in a Plexiglas annular container of height 100 mm, nominal radius $R = 44$ mm and gap-size $b = 7$ mm. The container is then filled to a depth $h = 65$ mm with ethanol 70% (see table 1 for the fluid properties). An air conditioning system helps in maintaining the temperature of the room at around 22°. The container is mounted on a loudspeaker VISATON TIW 360 8Ω placed on a flat table and connected to a wave generator TEKTRONIX AFG 1022, whose output signal is amplified using a wideband amplifier THURKBY THANDER WA301. The motion of the free surface is recorded with a digital camera NIKON D850 coupled with a 60mm f/2.8D lens and operated in slow motion mode, allowing for an acquisition frequency of 120 frames per second. A LED panel placed behind the apparatus provides back illumination of the fluid interface for better optimal contrast. The wave generator imposes a sinusoidal alternating voltage, $v = \left(\mathrm{V}_{pp}/2\right)\cos\left(\Omega t'\right)$, with $\Omega$ the angular frequency and $Vpp$ the full peak-to-peak voltage. The response of the loudspeaker to this input translates into a vertical harmonic motion of the container, $a\cos\left(\Omega t'\right)$, whose amplitude, $a$ [mm], is measured with a chromatic confocal displacement sensor STI CCS PRIMA/CLS-MG20. This optical pen, which is placed around 2 cm (within the admissible working range of 2.5 cm) above the container and points at the top flat surface of the outer container's wall, can detect the time-varying distance between the fixed sensor and the oscillating container's surface with a sampling rate in the order of

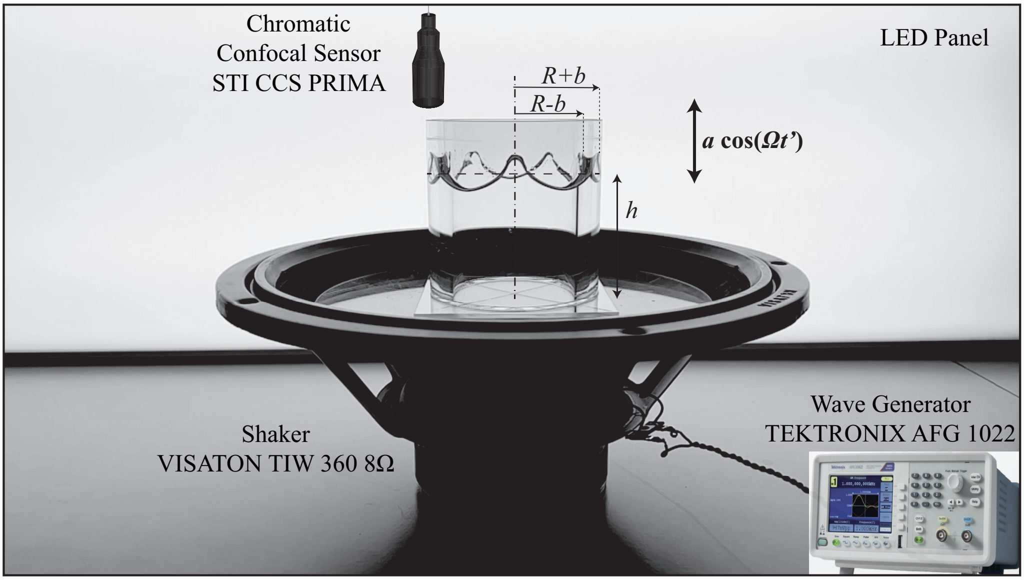


Figure 7: Photo of the experimental setup

kHz and a precision of ±1 $\mu$m. Thus, the pen can be used to obtain a very precise real-time value of $a$ as the voltage amplitude $Vpp$ and the frequency $\Omega$ are adjusted.

### 4.2. *Identification of the accessible experimental range*

Such a simple setup, however, put some constraints on the explorable experimental frequency range.

(i) First, we must ensure that the loudspeaker's output translates into a vertical container's displacement following a sinusoidal time signal. To this end, the optical sensor is used to measure the container motion at different driving frequencies. These time signals are then fitted with a sinusoidal law. Figure 8 shows how, below a forcing frequency of 8 Hz, the loudspeaker's output begins to depart from a sinusoidal signal. This check imposes a first lower bound on the explorable frequency range.

(ii) In addition, as Faraday waves only appear above a threshold amplitude, it is convenient to measure *a priori* the maximal vertical displacement $a$ achievable. The loudspeaker response curve is reported in the bottom part of figure 8. A superposition of this curve with the predicted Faraday's tongues immediately identifies the experimental frequency range within which the maximal achievable $a$ is larger than the predicted Faraday threshold so that standing waves are expected to emerge in our experiments. Assuming the herein proposed gap-averaged model (red regions) to give a good prediction of the actual instability onset, the experimental range explored in the next section is limited to approximately $\in [10.2, 15.6]$ Hz.

### 4.3. *Procedure*

Given the constraints discussed in §4.2, experiments have been carried out in a frequency range between 10.2 Hz and 15.6 Hz with a frequency step of 0.1 Hz. For each fixed forcing frequency, the Faraday threshold is determined as follows: the forcing amplitude $a$ is set to the maximal value achievable by the loudspeaker so as to trigger the emergence of the unstable Faraday wave quickly. The amplitude is then progressively decreased until the wave disappears and the surface becomes flat again.

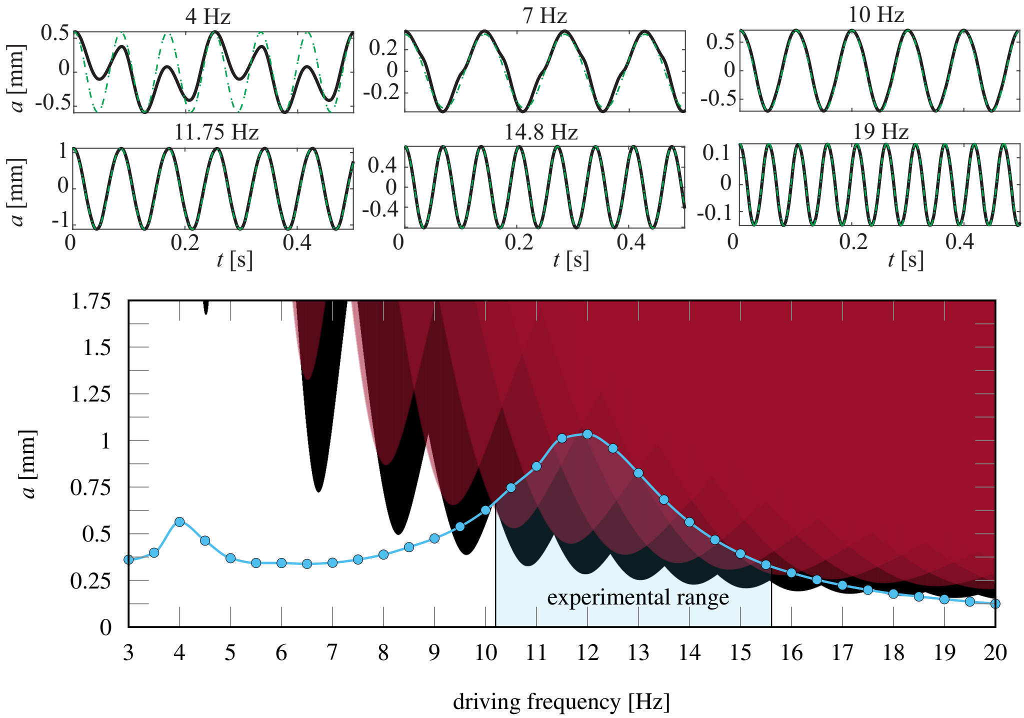


Figure 8: *Top*: vertical container displacement $a$ versus time at different forcing frequencies. The black curves are the measured signal, while the green dash-dotted curves are sinusoidal fitting. Below a forcing frequency of 8 Hz, the loudspeaker's output begins to depart from a sinusoidal signal. *Bottom*: sub-harmonic Faraday tongues computed by accounting for contact line dissipation with a mobility parameter $M = 0.0485$. The light blue curve here superposed corresponds to the maximal vertical displacement $a$ achievable with our setup. With this constraint, Faraday waves are expected to be observable only in the frequency range highlighted in blue.

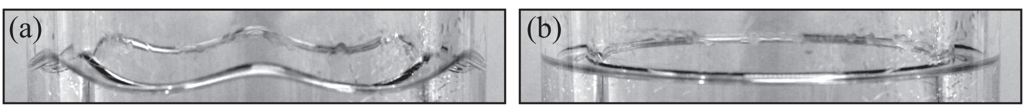


Figure 9: Free surface shape at a forcing frequency $1/T = 11.7$ Hz ($T$: forcing period) and corresponding to: (a) the lowest forcing amplitude value, $a = 0.4693$ mm, for which the $m = 6$ standing wave is present (the figure shows a temporal snapshot); (b) the largest forcing amplitude value, $a = 0.4158$ mm, for which the surface becomes flat and stable again. Despite the small forcing amplitude variation, the change in amplitude is large enough to allow for a visual inspection of the instability threshold with sufficient accuracy.

More precisely, a first quick pass across the threshold is made to determine an estimate of the sought amplitude. A second pass is then made by starting again from the maximum amplitude and decreasing it. When we approach the value determined during the first pass, we perform finer amplitude decrements, and we wait several minutes between each amplitude change to ensure that the wave stably persists. We eventually identify two values: the last amplitude where the instabilities were present (see figure 9(a)) and the first one where the surface becomes flat again (see figure 9(b)). Two more runs following an identical procedure are then performed to verify previously found values. Lastly, an average between

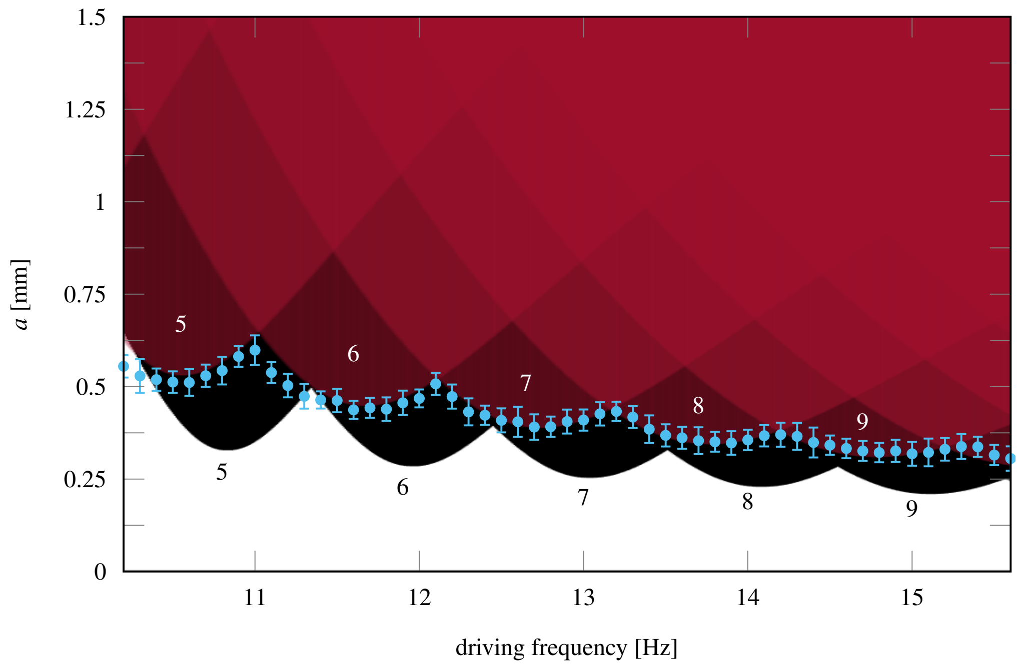


Figure 10: Experiments (empty circles) are compared to the theoretically predicted sub-harmonic Faraday threshold computed via Floquet analysis (2.32) for different fixed azimuthal wavenumber $m$ and according to the standard (black solid lines) and revised (red regions) gap-averaged models. The tongues are computed by including contact line dissipation with a value of $M$ equal to 0.0485 as in figure 6(b) and 8. As explained in §4.3, the vertical error bars indicate the amplitude range between the smallest measured forcing amplitude at which the instability was detected and the largest one at which the surface remains stable and flat. These two limiting values are successively corrected by accounting for the optical pen's measurement error and the non-uniformity of the output signal of the loudspeaker.

the smallest unstable amplitude and the largest stable one gives us the desired threshold.

Once the threshold amplitude value is found for the considered frequency, the output of the wave generator is switched off, the frequency is changed, and the steps presented above are repeated for the new frequency. In this way, we always start from a stable configuration, limiting the possibility of nonlinear interaction between different modes.

For each forcing frequency, the two limiting amplitude values, identified as described above, are used to define the error bars reported in figure 10. Those error bars must also account for the optical pen's measurement error (0.1 $\mu$m), as well as the non-uniformity of the output signal. By looking at the measured average, minimum, and maximum amplitude values in the temporal output signal, it is noteworthy that the average value typically deviates from the minimum and maximum by around 10 $\mu$m. Consequently, we incorporate in the error bars this additional 10 $\mu$m of uncertainty in the value of $a$. The uncertainty in the frequency of the output signal is not included in the definition of the error bars, as it is tiny, on the order of 0.001 Hz.

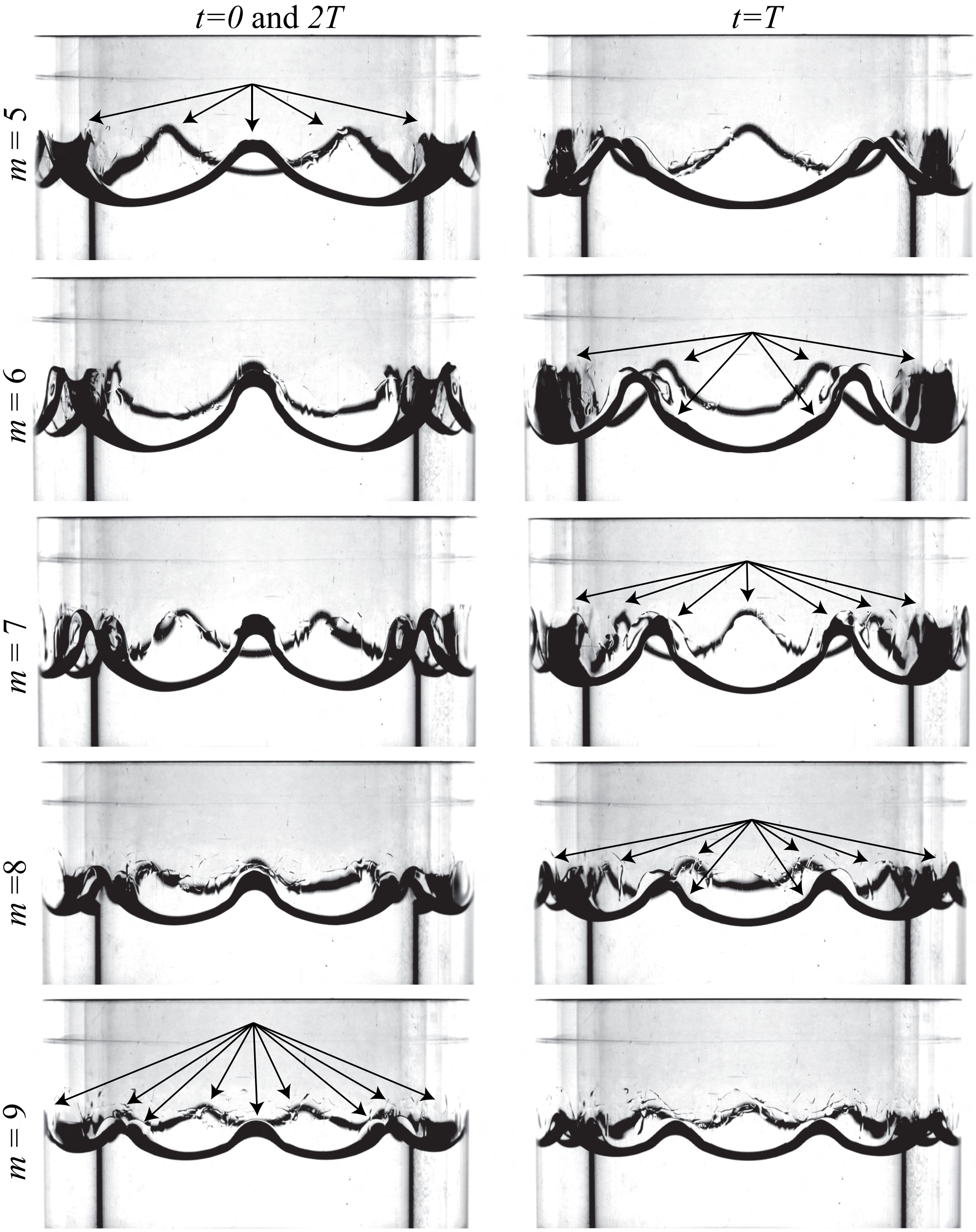


Figure 11: Snapshots of the wave patterns experimentally observed within the sub-harmonic Faraday tongues associated with the azimuthal wavenumbers $m = 5, 6, 7, 8$ and 9. $T$ is the forcing period, which is approximately half the oscillation period of the wave response. These patterns appear for: ($m = 5$) $1/T = 10.6$ Hz, $a = 0.8$ mm; ($m = 6$) $1/T = 11.6$ Hz, $a = 1.1$ mm; ($m = 7$) $1/T = 12.7$ Hz, $a = 0.9$ mm; ($m = 8$), $1/T = 13.7$ Hz, $a = 0.6$ mm; ($m = 9$) $1/T = 14.8$ Hz, $a = 0.4$ mm. These forcing amplitudes are the maximal achievable at their corresponding frequencies (see figure 8 for the associated operating points). The number of peaks is easily countable by visual inspection of two time-snapshots of the oscillating pattern extracted at $t = 0, T$ and $t = T/2$. This provides a simple criterion for the identification of the resonant wavenumber $m$. See also supplementary movies 1-5 at the link: [URL will be inserted by publisher].

### 4.4. *Instability onset and wave patterns*

The experimentally detected threshold at each measured frequency is reported in figure 10 in terms of forcing acceleration $f$ and amplitude $a$. Once again, the black unstable regions are calculated according to the standard gap-averaged model with $\sigma_{BL} = 12\nu/b^2$, whereas red regions are the unstable tongues computed using the modified damping $\sigma_{BL} = \chi_n \nu/b^2$. Both scenarios include contact line dissipation $\sigma_{CL} = (2M/\rho b)(m/R)\tanh(mh/R)$, with a value of $M$ equal to 0.0485 for ethanol 70%. Although, at first, this value has been selected in order to fit our experimental measurements, it is in perfect agreement with the linear relation linking $M$ to the liquid's surface tension reported in figure 5 of Hamraoui *et al.* (2000) and used by Li *et al.* (2019) (see table 1).

As figure 10 strikingly shows, the present theoretical thresholds match well our experimental measurements. On the contrary, the poor description of the oscillating boundary layer in the classical Darcy model translates into a lack of viscous dissipation. The arbitrary choice of a higher fitting parameter $M$ value, e.g. $M \approx 0.09$ would increase contact line dissipation and compensate for the underestimated Stokes boundary layer one, hence bringing these predictions much closer to experiments; however, such a value would lie well beyond the typical values reported in the literature. Furthermore, the real damping coefficient $\sigma_{BL} = 12\nu/b^2$ given by the Darcy theory does not account for the frequency detuning displayed by experiments. This frequency shift is instead well captured by the imaginary part of the new damping $\sigma_{BL} = \chi_n \nu/b^2$ (with $\chi_n = \chi_{n,r} + \mathrm{i}\chi_{n,i}$).

Within the experimental frequency range considered, five different standing waves, corresponding to $m = 5, 6, 7, 8$ and 9, have emerged. The identification of the wavenumber $m$ has been performed by visual inspection of the free surface patterns reported in figure 11. Indeed, by looking at a time snapshot, it is possible to count the various wave peaks along the azimuthal direction.

When looking at figure 10, it is worth commenting that on the left sides of the marginal stability boundaries associated with modes $m = 5$ and 6 we still have a little discrepancy between experiments and the model. Particularly, the experimental thresholds are slightly lower than the predicted ones. A possible explanation can be given by noticing that our experimental protocol is agnostic to the possibility of subcritical bifurcations and hysteresis, while such behaviour has been predicted by Douady (1990).

As a side comment, one must keep in mind that the Hele-Shaw approximation remains good only if the wavelength, $2\pi R/m$ does not become too small, i.e. comparable to the cell's gap, $b$. In other words, one must check that the ratio $mb/2\pi R$ is of the order of the small separation-of-scale parameter, $\epsilon$. For the largest wavenumber observed in our experiments, $m = 9$, the ratio $mb/2\pi R$ amounts to 0.23, which is not exactly small. Yet, the Hele-Shaw approximation is seen to remain fairly good.

The frequency detuning of the Faraday tongues is one of the main results of the present modified gap-averaged analysis. Although experiments match well the predicted sub-harmonic tongues reported in figure 10, other concomitant effects, such as a non-flat out-of-plane capillary meniscus, can contribute to shifting the natural frequencies and, consequently, the Faraday tongues, towards lower values (Douady 1990; Shao *et al.* 2021*b*). The present Floquet analysis assumes the static interface to be flat, although figure 9(b) shows that the stable free surface is not flat, but rather curved in the vicinity of the wall, where the meniscus height is approximately 1.5 mm. Bongarzone *et al.* (2022*b*) highlighted how a curved static interface can lower the natural frequencies. Since this effect has been ignored in the theoretical modelling, it is important to quantify such a frequency correction in relation to the one captured by the modified complex damping coefficient. This point is carefully addressed in Appendix C, where we demonstrate how the influence of a static

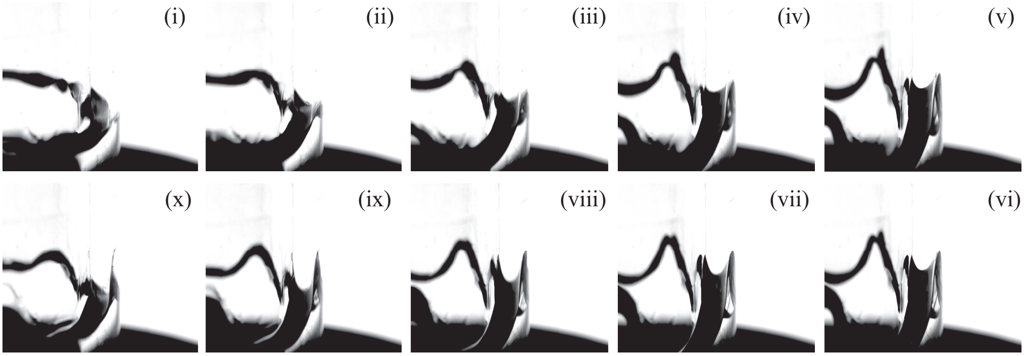


Figure 12: Zoom of the meniscus dynamics recorded at a driving frequency $1/11.6$ Hz and amplitude $a = 1.2$ mm for $m = 6$. Seven snapshots, (i)-(vii), covering one oscillation period, $T$, for the container motion are illustrated. These snapshots show how the meniscus profile and the macroscopic contact angle change in time during the second half of the advancing cycle and the first half of the receding cycle, hence highlighting the importance of the out-of-plane curvature or capillary effects. See also supplementary movie 6 at the link: [URL will be inserted by publisher].

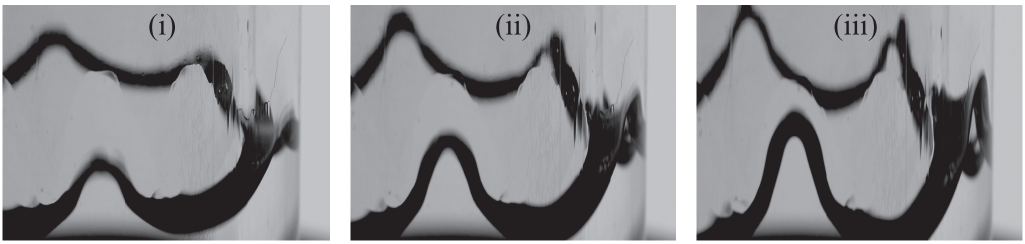


Figure 13: These three snapshots correspond to snapshots (ii), (iii) and (iv) of figure 12 and show, using a different light contrast, how the contact line constantly moves over a wetted substrate due to the presence of a stable thin film deposited and alimented at each cycle.

capillary meniscus does not significantly modify the natural frequencies of standing waves developing in the elongated (or azimuthal) direction.

### 4.5. *Contact angle variation and thin film deposition*

Before concluding, it is worth commenting on why the use of dynamic contact angle model (2.25) is justifiable and seen to give good estimates of the Faraday thresholds.

Existing lab experiments have revealed that liquid oscillations in Hele-Shaw cells constantly experience an up-and-down driving force with an apparent contact angle $\theta$ constantly changing (Jiang *et al.* 2004). Our experiments are consistent with such evidence. In figure 12, we report seven snapshots, (i)-(vii), covering one oscillation period, $T$, for the container motion. These snapshots illustrate a zoom of the dynamic meniscus profile and show how the macroscopic contact angle changes in time during the second half of the advancing cycle (i)-(v) and the first half of the receding cycle (vi)-(x), hence highlighting the importance of the out-of-plane meniscus curvature variations. Thus, on the basis of our observations, it seemed appropriate to introduce a contact angle model in the theory to justify this associated additional dissipation, which would be neglected by assuming $M = 0$. The model used in this study, and already implemented by Li *et al.* (2019), is very simple; it assumes the cosine of the dynamic contact angle to linearly depend on the capillary number $Ca$ (Hamraoui *et al.* 2000). Accounting for such a model is shown, both in Li *et al.* (2019) and in this study, to supplement the theoretical predictions by a sufficient extra dissipation suitable to match experimental measurements.

This dissipation eventually reduces to a simple damping coefficient $\sigma_{CL}$ as it is of linear nature. A unique constant value of the mobility parameter $M$ is sufficient to fit all our experimental measurements at once, suggesting that the meniscus dynamics is not significantly affected by the evolution of the wave in the azimuthal direction, i.e. by the wavenumber, and $M$ can be seen as an intrinsic property of the liquid-substrate interface.

Several studies have discussed the dependence of the system's dissipation on the substrate material (Huh & Scriven 1971; Dussan 1979; Cocciaro *et al.* 1993; Ting & Perlin 1995; Eral *et al.* 2013; Viola *et al.* 2018; Viola & Gallaire 2018; Xia & Steen 2018). These authors, among others, have unveiled and rationalised interesting features such as solid-like friction induced by contact angle hysteresis. This strongly nonlinear contact line behaviour does not seem to be present in our experiments. This can be tentatively explained by looking at figure 13. These snapshots illustrate how the contact line constantly flows over a wetted substrate due to the presence of a stable thin film deposited and alimented at each oscillation cycle. This feature has also been recently described by Dollet *et al.* (2020), who showed that the relaxation dynamics of liquid oscillation in a U-shaped tube filled with ethanol, due to the presence of a similar thin film, obey an exponential law that can be well-fitted by introducing a simple linear damping, as done in this work.

## 5. Conclusions

Previous theoretical analyses for Faraday waves in Hele-Shaw cells have so far relied on the Darcy approximation, which is based on the parabolic flow profile assumption in the narrow direction and that translates into a real-valued damping coefficient $\sigma_{BL} = 12\nu/b^2$, with $\nu$ the fluid kinematic viscosity and $b$ the cell's gap-size, that englobes the dissipation originated from the Stokes boundary layers over the two lateral walls. However, Darcy's model is known to be inaccurate whenever inertia is not negligible, e.g. in unsteady flows such as oscillating standing or travelling waves.

In this work, we have proposed a gap-averaged linear model that accounts for inertial effects induced by the unsteady terms in the Navier-Stokes equations, amounting to a pulsatile flow where the fluid motion reduces to a two-dimensional oscillating flow, reminiscent of the Womersley flow in cylindrical pipes. When gap-averaging the linearised Navier-Stokes equation, this results in a modified damping coefficient, $\sigma_{BL} = \chi_n \nu/b^2$, with $\chi_n = \chi_{n,r} + i\chi_{n,i}$ complex-valued, which is a function of the ratio between the Stokes boundary layer thickness and the cell's gap-size, and whose value depends on the frequency of the system's response specific to each unstable parametric Faraday tongue.

After having revisited the ideal case of infinitely long rectangular Hele-Shaw cells, for which we have found a good agreement against the experiments by Li *et al.* (2019), we have considered the case of Faraday waves in thin annuli. Due to the periodicity condition, this annular geometry naturally filters out the additional, although small, dissipation coming from the lateral wall in the elongated direction of finite-size lab-scale Hele-Shaw cells. Hence, a thin annulus offers a prototype configuration that can allow one to quantify better the correction introduced by the present gap-averaged theory when compared to dedicated experiments and to the standard gap-averaged Darcy model.

A series of homemade experiments for the latter configuration has proven that Darcy's model typically underestimates the Faraday threshold, as $\chi_{n,r} > 12$, and overlooks a frequency detuning introduced by $\chi_{n,i} > 0$, which appears essential to correctly predict the location of the Faraday's tongue in the frequency spectrum. The frequency-dependent gap-averaged model proposed here successfully predicts these features and brings the Faraday

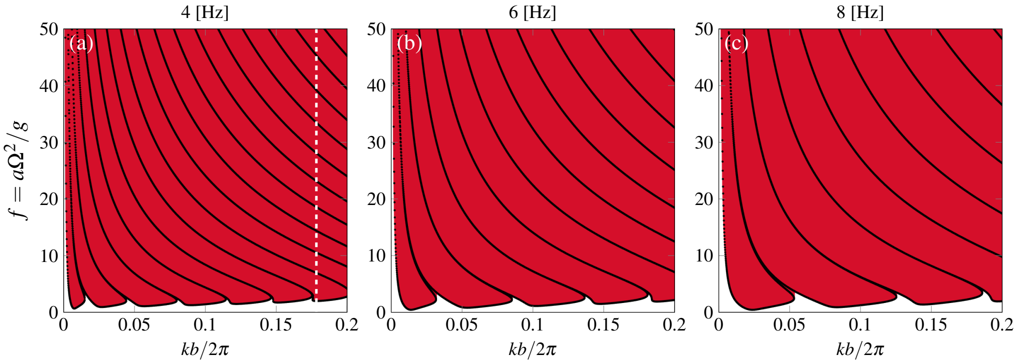


Figure 14: Same Faraday tongues of figure 3 by solving the eigenvalue problem (2.32) with $N = 10$ for three different fixed driving angular frequencies (reported on the top of each panel) and using the modified $\sigma_{BL} = \chi_n \nu / b^2$. Contact line dissipation is not included, i.e. $M = \sigma_{CL} = 0$. A much wider range of forcing acceleration, $f \leqslant 50$, is shown so as to give a more comprehensive view of the linear stability map. The convergence analysis outlined in table 2 is performed for the value of $kb/2\pi$ indicated by the vertical white dashed line, i.e. 0.178.

thresholds estimated theoretically closer to the ones measured.

Furthermore, a close look at the experimentally observed meniscus and contact angle dynamics highlighted the importance of the out-of-plane curvature, whose contribution has been neglected so far in the literature, with the exception of Li *et al.* (2019). This evidence justifies the employment of a dynamical contact angle model to recover the extra contact line dissipation and close the gap with experimental measurements.

A natural extension of this work is to examine the existence of a drift instability at higher forcing amplitudes.

## Appendix A. Convergence analysis as the truncation number $N$ varies

In §2.1, we have briefly described the procedure employed for solving the eigenvalue problem (2.32), where the structure of matrices **A** and **B** in the two cases of sub-harmonic and harmonic parametric resonances are given in Kumar & Tuckerman (1994). For each driving frequency and wavenumber, the eigenvalue problem is solved in Matlab using the built-in function *eigs*. Successively, by selecting one or several smallest, real positive values of $f$, one can draw the marginal stability boundaries of the various parametric tongues. For instance, those boundaries are indicated in figure 14 by the black dots, each of which corresponds to an eigenvalue $f$ for a fixed combination $(k, \Omega)$.

In order to ensure the numerical convergence of the results, the dependency of the eigenvalues on the truncation number $N$ must be checked. Throughout the paper, we have used a truncation number $N = 10$, which produces $2(N+1) \times 2(N+1) = 22 \times 22$ matrices. For their purposes, Kumar & Tuckerman (1994) used $N = 5$ or $N = 10$, which were sufficient to guarantee a good convergence. However, as the problem presented here differs from that tackled in Kumar & Tuckerman (1994), whether a similar truncation number, e.g. $N = 10$, is still sufficient needs to be verified.

A convergence analysis as $N$ varies is reported in table 2. The analysis is carried out with respect to the results already discussed in figure 3, but for a much wider range of forcing acceleration, $f = a\Omega^2/g$, which represents the eigenvalue of problem (2.32). The values of $f$ reported in table 2 are computed for a driving frequency of 4 Hz and for $kb/2\pi = 0.1783$,

| | | | | | | | | | | |
|---|---|---|---|---|---|---|---|---|---|---|
| Sub-Harmonic, $\xi_n = n + 1/2$, $n = 0, 1, 2, \ldots, N$ | | | | | | | | | | |
| $N = 5$ | 1.9517 | 6.9132 | 10.5310 | 15.0202 | 24.1264 | 70.3367 | – | – | – | – |
| $N = 6$ | 1.9517 | 6.9132 | 10.4992 | 14.3629 | 18.8594 | 25.6483 | 41.2706 | 121.3904 | – | – |
| $N = 7$ | 1.9517 | 6.9132 | 10.4990 | 14.3475 | 18.5500 | 23.2569 | 29.3149 | 39.6413 | 64.2494 | 190.0024 |
| $N = 8$ | 1.9517 | 6.9132 | 10.4990 | 14.3474 | 18.5435 | 23.1178 | 28.1327 | 34.0246 | 42.4155 | 57.5681 |
| $N = 9$ | 1.9517 | 6.9132 | 10.4990 | 14.3474 | 18.5434 | 23.1153 | 28.0740 | 33.4474 | 39.4465 | 47.0194 |
| $N = 10$ | 1.9517 | 6.9130 | 10.4990 | 14.3474 | 18.5434 | 23.1153 | 28.0731 | 33.4242 | 39.1782 | 45.4332 |
| $N = 15$ | 1.9517 | 6.9130 | 10.4990 | 14.3474 | 18.5434 | 23.1153 | 28.0731 | 33.4239 | 39.1694 | 45.3128 |
| $N = 20$ | 1.9517 | 6.9130 | 10.4990 | 14.3474 | 18.5434 | 23.1153 | 28.0731 | 33.4239 | 39.1694 | 45.3128 |
| Harmonic, $\xi_n = n$, $n = 1, 2, \ldots, N$ | | | | | | | | | | |
| $N = 5$ | | 6.9143 | 10.5916 | 15.8092 | 30.3987 | – | – | – | – | – |
| $N = 6$ | | 6.9134 | 10.4995 | 14.3927 | 19.2294 | 27.8359 | 53.9776 | – | – | – |
| $N = 7$ | | 6.9134 | 10.4988 | 14.3479 | 18.5629 | 23.4347 | 30.3688 | 44.0177 | 86.0342 | – |
| $N = 8$ | | 6.9134 | 10.4988 | 14.3475 | 18.5435 | 23.1232 | 28.2143 | 34.5709 | 44.5890 | 65.0100 |
| $N = 9$ | | 6.9134 | 10.4988 | 14.3475 | 18.5433 | 23.1155 | 28.0759 | 33.4827 | 39.7255 | 48.2205 |
| $N = 10$ | | 6.9134 | 10.4988 | 14.3475 | 18.5433 | 23.1154 | 28.0731 | 33.4250 | 39.1924 | 45.5686 |
| $N = 15$ | | 6.9134 | 10.4988 | 14.3475 | 18.5433 | 23.1154 | 28.0731 | 33.4239 | 39.1694 | 45.3129 |
| $N = 20$ | | 6.9134 | 10.4988 | 14.3475 | 18.5433 | 23.1154 | 28.0731 | 33.4239 | 39.1694 | 45.3129 |

Table 2: First smallest real positive eigenvalues, $f = a\Omega^2/g$ ($\leqslant 50$), outputted by the Floquet analysis at different truncation number $N$ for a fixed driving frequency of 4 Hz and for a fixed value of $kb/2\pi$, e.g. 0.178, as indicated by the vertical white dashed line in figure 14. The top table reports the values computed from the calculation of sub-harmonic (SH) tongues, whereas the bottom table reports those from the calculation of harmonic (H) tongues. The dash symbol, e.g. for $N = 5$, is used to indicate that no other real positive eigenvalues were found.

as indicated by the white dashed line in figure 14(a). Table 2 shows that a truncation number $N = 5$ is not sufficient to achieve convergence of the eigenvalues $f \leqslant 50$. Particularly, the algorithm does not succeed in finding many eigenvalues of interest as $N$ is too small to describe all the sub-harmonic and harmonic boundaries encountered at this value of $kb/2\pi$ for $f \leqslant 50$. Yet, $N = 5$ already provides a very high resolution of the first 2 or 3 eigenvalues for both sub-harmonic (SH) and harmonic tongues (H), which are sufficient to obtain the results discussed throughout the manuscript. The accuracy increases from $N = 5$ to $N = 9$ and the results for $N = 15$ or 20 confirm that a satisfactory convergence of all eigenvalues $f \leqslant 50$ is achieved for $N = 10$, with a maximum relative error $< 0.6\%$ .

## Appendix B. Sensitivity analysis to variations of the contact line parameter $M$

Although the introduction of the mobility parameter $M$ is not the central point of this paper, the effect of this parameter on the stability properties of Faraday waves in Hele-Shaw cells has not been fully elucidated yet. With regards to the sub-harmonic Faraday threshold in thin annuli discussed in §3 and §4, in this appendix, we carry out a sensitivity analysis of the instability onset to variations of $M$.

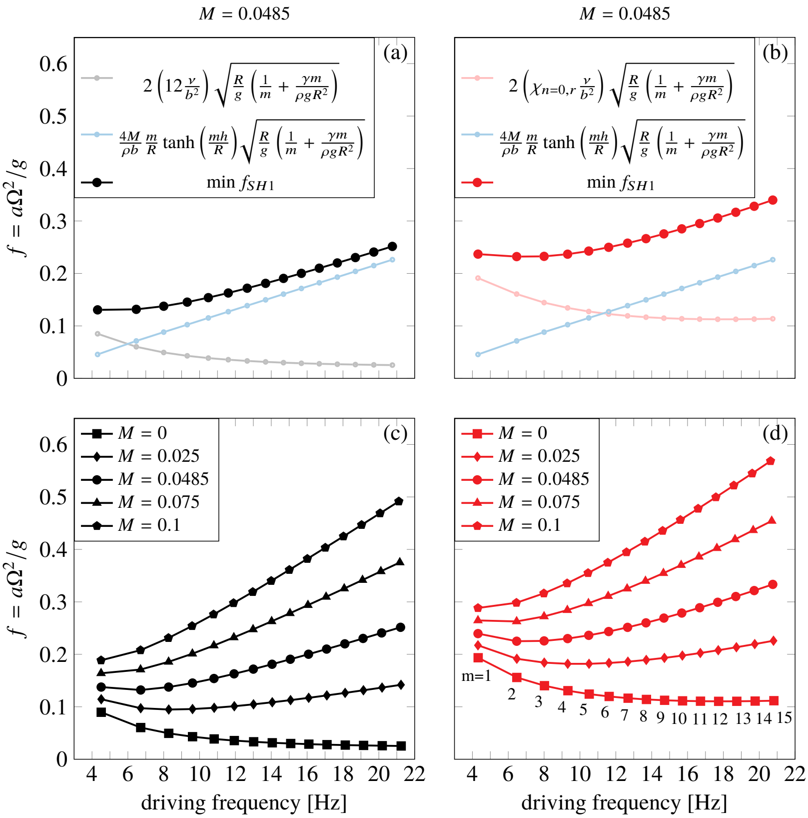


Figure 15: (a)-(b) Individual contributions, i.e. boundary layer and contact line ($M = 0.0485$), to the sub-harmonic onset acceleration of the first 15 azimuthal modes as prescribed by (B 2). (c)-(d) Onset acceleration of the first 15 azimuthal modes as prescribed by (B 2) for several values of $M$. Panels (a)-(c) use the boundary layer damping from the Darcy theory, while panels (b)-(d) use the modified damping coefficient presented in this work. Note that in each subpanel, the solid lines only serve to guide the eye.

The asymptotic approximation (3.9)

$$\min f_{SH1} \approx 2\sigma_{0,r}\sqrt{\frac{R}{g}\left(\frac{1}{m}+\frac{\gamma}{\rho g R^2}m\right)}, \tag{B 1}$$

gives us a simple analytical formula for the minimum onset acceleration $f_{SH1}$ associated with the first sub-harmonic parametric instability of a generic azimuthal mode $m$. Specifically, equation (B 1) helps us to rationalise the effect of interplaying restoring forces, i.e. gravity and capillarity, and dissipation sources, i.e. boundary layers and contact line, on the instability onset.

Recalling the definition of $\sigma_{0,r}$ from (2.27$a$), the onset acceleration is given by the sum of two contributions

$$\min f_{SH1} \approx 2\,\chi_{n=0,r}\frac{\nu}{b^2}\sqrt{\frac{R}{g}\left(\frac{1}{m}+\frac{\gamma}{\rho g R^2}m\right)} + \frac{4M}{\rho b}\frac{m}{R}\sqrt{\frac{R}{g}\left(\frac{1}{m}+\frac{\gamma}{\rho g R^2}m\right)}, \tag{B 2}$$

where the deep water approximation $\tanh(mh/R) \approx 1$ has been used for simplicity.

The two contributions and their sum are plotted in figure 15(a)-(b), where the filled circles correspond to the azimuthal wavenumbers reported in figure 6, i.e. $m = 1, 2, \ldots, 15$. The parameter $M$ is fixed to the value used in §3 and §4, i.e. 0.0485. In panel (a) the boundary layer damping is the one given by the Darcy theory, $12\nu/b^2$, whereas in panel (b) the modified damping coefficient $\chi_{n=0,r}\,\nu/b^2$ is used. In the absence of contact line dissipation, the onset acceleration of low $m$-modes progressively decreases as the threshold is dictated by the gravity term $\sim \sqrt{1/m}$, while capillarity only matters at larger $m$. On the contrary, assuming $M \neq 0$ introduces a correction $\sim \sqrt{m}$ that, depending on the value of $M$, may quickly dominate over $\sqrt{1/m}$, hence leading to a growing min $f_{SH1}$ already at relatively low $m$. Such a trend is exacerbated by larger $M$. This is clearly visible in figure 15(c)-(d), where only the overall value min $f_{SH1}$ is plotted for several values of $M$.

The exact same arguments apply as well to the case of rectangular Hele-Shaw cells with the only difference that $m/R \to k$. A similar trend of min $f_{SH1}$ for increasing driving frequencies is indeed observable in figure 5.

## Appendix C. Modification of the unforced dispersion relation due to a non-flat out-of-plane capillary meniscus

The revised gap-averaged Floquet analysis formalized in this work provides a modified damping coefficient, $\sigma_{CL} = \chi_n \nu/b^2$ with $\chi_n \in \mathbb{C}$, whose imaginary part $\chi_{n,i} > 0$ leads to a frequency detuning of the Faraday tongues. This detuning represents one of the main findings of the analysis and seems confirmed by our experimental observations.

However, there may be other concomitant effects ignored by the analysis, such as a non-flat out-of-plane capillary meniscus, that could contribute to shifting the natural frequencies and, consequently, the Faraday tongues, towards lower values, thus possibly questioning the actual improvement brought by the present theory. Bongarzone *et al.* (2022*b*) highlighted how a curved static interface lowers the resonant frequencies. Since this effect has been ignored in our theoretical model, it is important to quantify such a frequency shift in relation to the one produced by the oscillating boundary layer, so as to verify that the detuning is actually produced by the oscillating viscous boundary layers rather than by static capillary effects.

A way to disentangle the latter contribution from the former one consists in estimating the inviscid natural frequencies when a static meniscus is present. This Appendix, which is inspired by the work of Monsalve *et al.* (2022), aims precisely to address this point. Specifically, some of the results reported in Monsalve *et al.* (2022) will be used in figure 16(a)-(c) as a validation of the numerical method employed in the following.

Note that the analysis is carried out for transverse waves with wavenumber $k$ in a rectangular channel, but it also applies to azimuthal waves with wavenumber $m$ in thin annular channels. Indeed, we have shown in §3 that for small gap-sizes $b$ the governing equations in the two cases coincide, with the only difference that $k$ becomes $m/R$ and $m = 1, 2, \ldots$, i.e. for a fixed radius $R$, the wavenumber is discrete.

The first step consists of computing the shape of the actual two-dimensional static meniscus, whose governing equation balances gravity and capillarity

$$\rho g \eta_s' = \gamma \kappa' \left(\eta_s'\right) = \gamma \frac{\eta'_{s,y'y'}}{\left(1 + \eta'^2_{s,y'}\right)^{3/2}}, \qquad \text{with} \qquad \left.\frac{\partial \eta_s'}{\partial y'}\right|_{y'=\pm b/2} = \cot\theta_s. \tag{C 1}$$

Note that the shape of the meniscus is assumed invariant in the elongated direction $x'$ (or $\varphi$) so that $\eta'_{s,x'} = \eta'_{s,x'x'} = 0$ ($x' \leftrightarrow \varphi$):

$$\kappa'\left(\eta'_s\right) = \frac{\eta'_{s,x'x'}\left(1+\eta'^2_{s,y'}\right) + \eta'_{s,y'y'}\left(1+\eta'^2_{s,x'}\right) - 2\eta'_{s,x'}\eta'_{s,y'}\eta'_{s,x'y'}}{\left(1+\eta'^2_{s,x'}+\eta'^2_{s,y'}\right)^{3/2}} = \frac{\eta'_{s,y'y'}}{\left(1+\eta'^2_{s,y}\right)^{3/2}}. \tag{C 2}$$

Equation (C 1) is nonlinear in $\eta'_s$ and is solved numerically in Matlab through a Chebyshev collocation method and the Gauss–Lobatto–Chebyshev collocation grid $s \in [-1, 1]$ is mapped into the physical space $y' \in [0, b/2]$ through the linear mapping $y' = (s+1)b/4$. Hence the solution to the nonlinear equation is obtained by means of an iterative Newton method, whose detailed steps are given in Appendix A.1 of Viola *et al.* (2018).

Figure 9(b) shows that the stable free surface is not flat, but rather curved in the vicinity of the wall, where the meniscus height is approximately 1.5 mm. Given the fluid properties of ethanol 70%, we can fit the value of the static contact angle in order to retrieve the measured meniscus height. The results of this procedure are given in figure 16(b), which displays the shape of the static out-of-plane capillary meniscus corresponding to our experiments. A static angle $\theta_s = 28°$, which coincides with the value measured by Dollet *et al.* (2020), is found to give the correct meniscus height at the wall.

Next, we introduce the velocity potential $\Phi'$ and write down the potential form of the unforced governing equations and boundary conditions introduced in §2. Those equations are linearized around the rest state, which has now a curved static interface in the direction of the small gap-size, i.e. $\eta'_s(y) \neq 0$. The continuity equation rewrites as the Laplacian of the velocity potential

$$-k^2\check{\Phi}' + \frac{\partial^2\check{\Phi}'}{\partial y'^2} + \frac{\partial^2\check{\Phi}'}{\partial z'^2} = 0, \tag{C 3}$$

subjected to the no-penetration condition at the solid bottoms and lateral walls $\partial\check{\Phi}'/\partial n' = 0$, while the dynamic and kinematic conditions read

$$\mathrm{i}\omega_0\check{\Phi}' = -g\check{\eta}' + \frac{\gamma}{\rho}\left[\frac{1}{\left(1+\eta'^2_{s,y'}\right)^{3/2}}\frac{\partial^2}{\partial y'^2} - \frac{3\eta'_{s,y'y'}\eta'_{s,y'}}{\left(1+\eta'_{s,y'}\right)^{5/2}}\frac{\partial}{\partial y'} - \frac{k^2}{\left(1+\eta'^2_{s,y'}\right)^{1/2}}\right]\check{\eta}', \tag{C 4}$$

$$\mathrm{i}\omega_0\check{\eta}' = \frac{\partial\check{\Phi}'}{\partial z'}, \tag{C 5}$$

where the following ansatzes for the infinitesimal perturbations

$$\Phi' = \check{\Phi}'(y', z')\, e^{\mathrm{i}(\omega_0 t' + kx')} + c.c., \qquad \eta' = \check{\eta}'(y')\, e^{\mathrm{i}(\omega_0 t' + kx')} + c.c., \tag{C 6}$$

have been introduced. In order to close the problem we enforced a contact line condition

$$\left.\frac{\partial\check{\eta}'}{\partial y'}\right|_{y'=\pm b/2} = 0 \quad \text{(free)} \quad \text{or} \quad \left.\frac{\partial\check{\eta}'}{\partial t'}\right|_{y'=\pm b/2} = 0 \quad \text{(pinned)}. \tag{C 7}$$

Conditions (C 7) represent two diametrically opposed scenarios. The most relevant condition to be considered for our experiments is the free contact line, but the results obtained from the imposition of the pinned contact line condition are used for validation with Monsalve *et al.* (2022). Regardless of the chosen contact line condition (C 7), equations (C 3)-(C 8) can be recast into the generalized eigenvalue problem

$$\left(\mathrm{i}\omega_0\mathcal{B} - \mathcal{A}_k\right)\check{\mathbf{q}}' = 0, \tag{C 8}$$

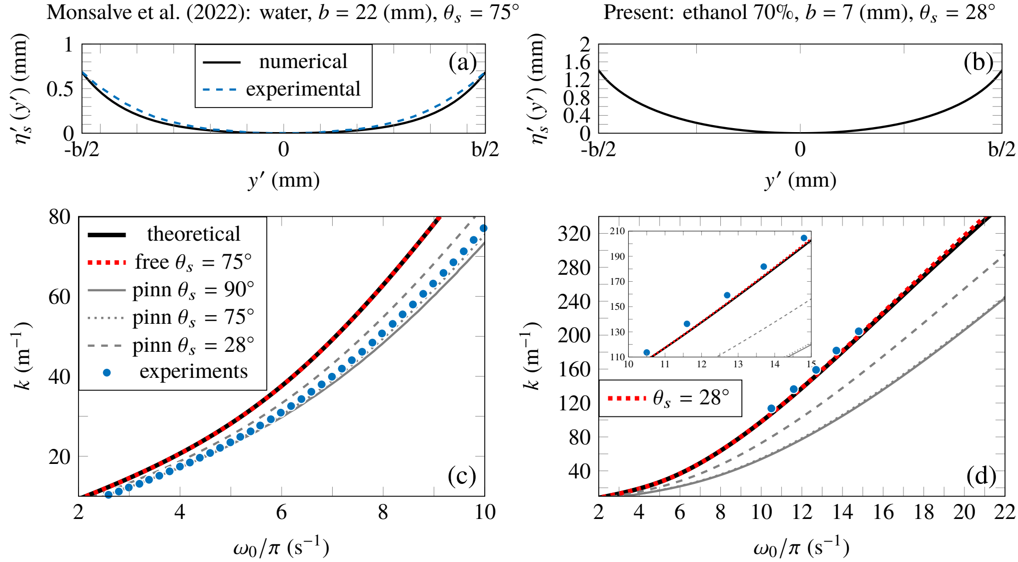


Figure 16: (a) Static meniscus measured experimentally by Monsalve *et al.* (2022) using water and a gap-size $b = 22$ mm (dashed line) and computed numerically according to (C 1) using a value of $\theta_s = 75°$. (b) Shape of the static meniscus computed numerically in our experimental setup. (c) Black solid line: theoretical dispersion relation for the case of water, fluid depth $h = 50$ mm and $b = 22$ mm, $\omega_0^2 = \left(1 + \gamma k^2/\rho g\right) gk \tanh kh$. Grey solid line: numerical dispersion relation in the case of a pinned contact line. Red dotted, grey dotted and grey dashed lines give the meniscus corrections to the two dispersion relations, while the blue filled circles correspond to the experiments of Monsalve *et al.* (2022) with a pinned contact line and with the static meniscus reported in panel (a). A comparison of this panel (c) to figure 8 of Monsalve *et al.* (2022) validates our numerical scheme. Their curves are not reported for the sake of clarity but perfectly overlap our curves. (d) Same as in (c), but for the condition of our experimental setup. The blue-filled circles correspond to the driving frequency associated with the minimal onset acceleration amplitude for modes $m = 5, 6, 7, 8$ and 9 for which $k = m/R$ ($R = 44$ mm). The inset shows that the meniscus correction to the frequency, being negligible, does not explain the frequency shift of the experimental Faraday tongues. Indeed, the blue markers lie above all dispersion relations obtained by varying the static contact angle and wetting conditions.

with $\check{\mathbf{q}}' = \left\{\check{\Phi}', \check{\eta}'\right\}^T$ a natural mode of the system and $\omega_0$ the associated natural frequency. The expression of linear operators $\mathcal{B}$ and $\mathcal{A}_k$ is given in Viola *et al.* (2018).Those operators are here discretized by means of the Chebyshev collocation method, where a two-dimensional mapping is used to map the computational space to the physical space that has a curved boundary due to the static meniscus $\eta_s'$. The eigenvalue problem (C 8) is then solved numerically in Matlab using the built-in function *eigs* by providing the wavenumber $k$ as an input. The number of grid points in the radial and vertical direction is $n_y = n_z = 60$, which largely ensures convergence of the results. This numerical approach has been employed and validated in a series of recent works (Bongarzone *et al.* 2022*a*; Marcotte *et al.* 2023*a*,*b*), and a detailed description of its implementation can be found in Appendix A.2 of Viola *et al.* (2018).

The modified dispersion relation of transverse (or azimuthal) wave computed numerically by solving (C 8) is displayed in figure 16(c)-(d). Panel (c) reproduces figure 8 of Monsalve *et al.* (2022) and only serves as a further validation step for our numerical method. Instead, panel (d) shows that our measurements (blue markers) lie above all dispersion relations obtained by varying the static contact angle and wetting conditions. In other words, the nose of the Faraday tongues are found at frequencies lower than any of those obtained by accounting for the meniscus shape and the wetting conditions, irrespective of the latter. This indicates that another mechanism accounts for this frequency shift. Since in addition, in the free contact line regime, the static contact angle does not have a perceivable effect, the entirety of the frequency shift has to be accounted for by another effect, which we show to possibly be unsteady boundary layers.

Panels (c) and (d) both show that meniscus modifications are much more pronounced, at least at low $\theta_s$ values, when the contact line remains pinned at the lateral walls. This is somewhat intuitive as the first-order interface shape strongly depends on the $y'$-coordinate (see figure 5 of Monsalve *et al.* (2022)), whereas it is almost invariant in $y'$ if the contact line follows a free dynamics. Given that in our experiments the contact line follows a free dynamics, we can eventually justify ignoring the shape of the out-of-plane capillary meniscus. On the other hand, the actual shape of the static meniscus is important for pinned contact line conditions, as it provokes a non-negligible increase of the natural frequencies (Wilson *et al.* 2022).

## Supplementary Material

Supplementary movies 1-5 show the time evolution of the free surface associated with the snapshots reported in figure 11. Supplementary movie 6 provides instead a better visualisation of the meniscus and the thin film dynamics as illustrated in figures 12 and 13 of this manuscript. Supplementary movies are available at the link: [URL will be inserted by publisher].

## Acknowledgements

We acknowledge Simeon V. Djambov for the fruitful discussion about the meniscus dynamics in the Hele-Shaw limit.

## Funding

We acknowledge the Swiss National Science Foundation under grant 178971.

## Declaration of Interests

The authors report no conflict of interest.

## Author Contributions

A. B., F. V. and F. G. created the research plan. A.B. formulated analytical and numerical models. A.B. led model solution. A. B. and B. J. designed the experimental setup. B. J. performed all experiments. A.B., F.V. and F.G. wrote the manuscript.

## REFERENCES

Afkhami, S. & Renardy, Y. 2013 A volume-of-fluid formulation for the study of co-flowing fluids governed by the hele-shaw equations. *Phys. Fluids* **25** (8), 082001.

Batson, W., Zoueshtiagh, F. & Narayanan, R. 2013 The faraday threshold in small cylinders and the sidewall non-ideality. *J. Fluid Mech.* **729** (496-523), 9.

Bechhoefer, J., Ego, V., Manneville, S. & Johnson, B. 1995 An experimental study of the onset of parametrically pumped surface waves in viscous fluids. *J. Fluid Mech.* **288**, 325–350.

Benjamin, T. B. & Scott, J. C. 1979 Gravity-capillary waves with edge constraints. *J. Fluid Mech.* **92**, 241–267.

Benjamin, T. B. & Ursell, F. J. 1954 The stability of the plane free surface of a liquid in vertical periodic motion. *Proc. R. Soc. Lond. A* **225** (1163), 505–515.

Blake, T. D. 1993 Dynamic contact angle and wetting kinetics. *Wettability* .

Blake, T. D. 2006 The physics of moving wetting lines. *J. Colloid Interface Sci.* **299** (1), 1–13.

Bongarzone, A., Guido, M. & Gallaire, F. 2022*a* An amplitude equation modelling the double-crest swirling in orbital-shaken cylindrical containers. *J. Fluid Mech.* **943**, A28.

Bongarzone, A., Viola, F., Camarri, S. & Gallaire, F. 2022*b* Subharmonic parametric instability in nearly brimful circular cylinders: a weakly nonlinear analysis. *J. Fluid Mech.* **947**, A24.

Bongarzone, A., Viola, F. & Gallaire, F. 2021 Relaxation of capillary-gravity waves due to contact line nonlinearity: A projection method. *Chaos* **31** (12), 123124.

Chuoke, R. L., Meurs, P. Van & van der Poel, C. 1959 The instability of slow, immiscible, viscous liquid-liquid displacements in permeable media. *Trans. Am. Inst.* **216** (01), 188–194.

Cocciaro, B., Faetti, S. & Festa, C. 1993 Experimental investigation of capillarity effects on surface gravity waves: non-wetting boundary conditions. *J. Fluid Mech.* **246**, 43–66.

Dollet, B., Lorenceau, É. & Gallaire, F. 2020 Transition from exponentially damped to finite-time arrest liquid oscillations induced by contact line hysteresis. *Phys. Rev. Lett.* **124** (10), 104502.

Douady, S. 1990 Experimental study of the Faraday instability. *J. Fluid Mech.* **221**, 383–409.

Douady, S., Fauve, S. & Thual, O. 1989 Oscillatory phase modulation of parametrically forced surface waves. *EPL* **10** (4), 309.

Dussan, E. B. 1979 On the spreading of liquids on solid surfaces: static and dynamic contact lines. *Ann. Rev. Fluid Mech.* **11** (1), 371–400.

Eral, H. B., Mannetje, J. C. M. 'T & Oh, J. M. 2013 Contact angle hysteresis: a review of fundamentals and applications. *Colloid Polym. Sci.* **291** (2), 247–260.

Faraday, M. 1831 *Phil. Trans.* .

Fauve, S., Douady, S. & Thual, O. 1991 Drift instabilities of cellular patterns. *J. Phys. II* **1** (3), 311–322.

Gondret, P. & Rabaud, M. 1997 Shear instability of two-fluid parallel flow in a hele–shaw cell. *Phys. Fluids* **9** (11), 3267–3274.

Graham-Eagle, J. 1983 A new method for calculating eigenvalues with applications to gravity-capillary waves with edge constraints. *Math. Proc. Camb. Phil. Soc.* **94** (3), 553–564.

Hamraoui, A., Thuresson, K., Nylander, T. & Yaminsky, V. 2000 Can a dynamic contact angle be understood in terms of a friction coefficient? *J. Colloid Interface Sci.* **226** (2), 199–204.

Henderson, D. M. & Miles, J. W. 1990 Single-mode faraday waves in small cylinders. *J. Fluid Mech.* **213**, 95–109.

Henderson, D. M. & Miles, J. W. 1994 Surface-wave damping in a circular cylinder with a fixed contact line. *J. Fluid Mech.* **275**, 285–299.

Hocking, L. M. 1987 The damping of capillary–gravity waves at a rigid boundary. *J. Fluid Mech.* **179**, 253–266.

Howell, D. R., Buhrow, B., Heath, T., McKenna, C., Hwang, W. & Schatz, M. F. 2000 Measurements of surface-wave damping in a container. *Phys. Fluids* **12** (2), 322–326.

Huh, C. & Scriven, L. E. 1971 Hydrodynamic model of steady movement of a solid/liquid/fluid contact line. *J. Colloiud. Interf. Sci.* **35** (1), 85–101.

Jiang, L., Perlin, M. & Schultz, W. W. 2004 Contact-line dynamics and damping for oscillating free surface flows. *Phys. Fluids* **16** (3), 748–758.

Johansson, P. & Hess, B. 2018 Molecular origin of contact line friction in dynamic wetting. *Phys. Rev. Fluids* **3** (7), 074201.

Kalogirou, A., Moulopoulou, E. E. & Bokhove, O. 2016 Variational finite element methods for waves in a hele-shaw tank. *App. Math. Model.* **40** (17-18), 7493–7503.

Kumar, K. & Tuckerman, L. S. 1994 Parametric instability of the interface between two fluids. *J. Fluid Mech.* **279**, 49–68.

Lamb, H. 1993 *Hydrodynamics*. Cambridge University Press.

Li, J., Li, X., hen, K., Xie, B. & Liao, S. 2018*a* Faraday waves in a hele-shaw cell. *Phys. Fluids* **30** (4), 042106.

Li, J., Li, X. & Liao, S. 2019 Stability and hysteresis of faraday waves in hele-shaw cells. *J. Fluid Mech.* **871**, 694–716.

Li, X., Li, J., Liao, S. & Chen, C. 2018*b* Effect of depth on the properties of two coupled faraday waves in a hele-shaw cell. *Phys. Fluids* **30** (10), 102103.

Li, X., Li, X. & Liao, S. 2016 Pattern transition of two-dimensional faraday waves at an extremely shallow depth. *Sci. China Phys. Mech.* **59**, 1–3.

Li, X., Xu, D. & Liao, S. 2014 Observations of highly localized oscillons with multiple crests and troughs. *Phys. Rev. E* **90** (3), 031001.

Li, X., Yu, Z. & Liao, S. 2015 Observation of two-dimensional faraday waves in extremely shallow depth. *Phys. Rev. E* **92** (3), 033014.

Luchini, P. & Charru, F. 2010 Consistent section-averaged equations of quasi-one-dimensional laminar flow. *J. Fluid Mech.* **656**, 337–341.

Marcotte, A., Gallaire, F. & Bongarzone, A. 2023*a* Super-harmonically resonant swirling waves in longitudinally forced circular cylinders. *J. Fluid Mech.* **966**, A41.

Marcotte, Alice, Gallaire, François & Bongarzone, Alessandro 2023*b* Swirling against the forcing: evidence of stable counter-directed sloshing waves in orbital-shaken reservoirs, arXiv: 2302.14579.

McLean, J. W. & Saffman, P. G. 1981 The effect of surface tension on the shape of fingers in a hele-shaw cell. *J. Fluid Mech.* **102**, 455–469.

Miles, J. W. 1990 Capillary-viscous forcing of surface waves. *J. Fluid Mech.* **219**, 635–646.

Monsalve, E., Maurel, A., Pagneux, V. & Petitjeans, P. 2022 Space-time-resolved measurements of the effect of pinned contact line on the dispersion relation of water waves. *Phys. Rev. Fluids* **7** (1), 014802.

Müller, H. W., Wittmer, H., Wagner, C., Albers, J. & Knorr, K. 1997 Analytic stability theory for faraday waves and the observation of the harmonic surface response. *Phys. Rev. Lett.* **78** (12), 2357.

Nayfeh, A. H. 2008 *Perturbation Methods*. Wiley.

Park, C.-W. & Homsy, G. M. 1984 Two-phase displacement in hele shaw cells: theory. *J. Fluid Mech.* **139**, 291–308.

Périnet, N., Falcón, C., Chergui, J., Juric, D. & Shin, S. 2016 Hysteretic faraday waves. *Phys. Rev. E* **93** (6), 063114.

Plouraboué, F. & Hinch, E. J. 2002 Kelvin–helmholtz instability in a hele-shaw cell. *Phys. Fluids* **14** (3), 922–929.

Popinet, S. 2003 Gerris: a tree-based adaptive solver for the incompressible euler equations in complex geometries. *J. Comp. Physics* **190** (2), 572–600.

Popinet, S. 2009 An accurate adaptive solver for surface-tension-driven interfacial flows. *J. Comp. Physics* **228** (16), 5838–5866.

Rachik, A. & Aniss, S. 2023 Effects of finite depth and surface tension on the linear and weakly non-linear stability of faraday waves in hele-shaw cell. *Fluid Dyn. Res.* **55** (4), 045506.

Rajchenbach, J. & Clamond, D. 2015 Faraday waves: their dispersion relation, nature of bifurcation and wavenumber selection revisited. *J. Fluid Mech.* **777**, R2.

Rajchenbach, J., Leroux, A. & Clamond, D. 2011 New standing solitary waves in water. *Phys. Rev. Lett.* **107** (2), 024502.

Ruyer-Quil, C. 2001 Inertial corrections to the darcy law in a hele–shaw cell. *Comptes Rendus de l'Académie des Sciences-Series IIB-Mechanics* **329** (5), 337–342.

Saffman, P. G. & Taylor, G. I. 1958 The penetration of a fluid into a porous medium or hele-shaw cell containing a more viscous liquid. *Proc. R. Soc. A: Math. Phys. Eng. Sci.* **245** (1242), 312–329.

San, Omer & Staples, Anne E 2012 An improved model for reduced-order physiological fluid flows. *J. Mech. Med. Biol.* **12** (03), 1250052.

Schwartz, L. 1986 Stability of hele–shaw flows: The wetting-layer effect. *Phys. Fluids* **29** (9), 3086–3088.

Shao, X., Gabbard, C. T., Bostwick, J. B. & Saylor, J. R. 2021*a* On the role of meniscus geometry in capillary wave generation. *Exp. Fluids* **62** (3), 1–4.

Shao, X., Wilson, P., Saylor, J. R. & Bostwick, J. B. 2021*b* Surface wave pattern formation in a cylindrical container. *J. Fluid Mech.* **915**.

Ting, C. L. & Perlin, M. 1995 Boundary conditions in the vicinity of the contact line at a vertically oscillating upright plate: an experimental investigation. *J. Fluid Mech.* **295**, 263–300.

Ubal, S., Giavedoni, M. D. & Saita, F. A. 2003 A numerical analysis of the influence of the liquid depth on two-dimensional faraday waves. *Phys. Fluids* **15** (10), 3099–3113.

Viola, F., Brun, P.-T. & Gallaire, F. 2018 Capillary hysteresis in sloshing dynamics: a weakly nonlinear analysis. *J. Fluid Mech.* **837**, 788–818.

Viola, F. & Gallaire, F. 2018 Theoretical framework to analyze the combined effect of surface tension and viscosity on the damping rate of sloshing waves. *Phys. Rev. Fluids* **3** (9), 094801.

Viola, F., Gallaire, F. & Dollet, B. 2017 Sloshing in a hele-shaw cell: experiments and theory. *J. Fluid Mech.* **831**.

Voinov, O. V. 1976 Hydrodynamics of wetting. *Fluid Dyn.* **11** (5), 714–721.

Ward, K., Zoueshtiagh, F. & Narayanan, R. 2019 Faraday instability in double-interface fluid layers. *Phys. Rev. Fluids* **4**, 043903.

Wilson, P., Shao, X., Saylor, J. R. & Bostwick, J. B. 2022 Role of edge effects and fluid depth in azimuthal faraday waves. *Phys. Rev. Fluids* **7**, 014803.

Womersley, J. R. 1955 Method for the calculation of velocity, rate of flow and viscous drag in arteries when the pressure gradient is known. *Physiol. J.* **127** (3), 553.

Xia, Y. & Steen, P. H. 2018 Moving contact-line mobility measured. *J. Fluid Mech.* **841**, 767–783.